



UNIVERSITY OF LEEDS

This is a repository copy of *Analytical forecasting of long-term railway track settlement*.

White Rose Research Online URL for this paper:

<https://eprints.whiterose.ac.uk/182751/>

Version: Accepted Version

Article:

Charoenwong, C, Connolly, DP, Woodward, PK et al. (2 more authors) (2022) Analytical forecasting of long-term railway track settlement. *Computers and Geotechnics*, 143. 104601. ISSN 0266-352X

<https://doi.org/10.1016/j.compgeo.2021.104601>

© 2021, Elsevier. This manuscript version is made available under the CC-BY-NC-ND 4.0 license <http://creativecommons.org/licenses/by-nc-nd/4.0/>.

Reuse

This article is distributed under the terms of the Creative Commons Attribution-NonCommercial-NoDerivs (CC BY-NC-ND) licence. This licence only allows you to download this work and share it with others as long as you credit the authors, but you can't change the article in any way or use it commercially. More information and the full terms of the licence here: <https://creativecommons.org/licenses/>

Takedown

If you consider content in White Rose Research Online to be in breach of UK law, please notify us by emailing eprints@whiterose.ac.uk including the URL of the record and the reason for the withdrawal request.



eprints@whiterose.ac.uk
<https://eprints.whiterose.ac.uk/>

1 **Title:** Analytical forecasting of long-term railway track settlement

2 **C. Charoenwong^a, D.P. Connolly^{a,*}, P.K. Woodward^a, P. Galvín^{b,c}, P. Alves Costa^d**

3 ^a *Institute for High Speed Rail and Systems Integration, School of Civil Engineering, University*
4 *of Leeds, UK*

5 ^b *Escuela Técnica Superior de Ingeniería, Universidad de Sevilla, Camino de los*
6 *Descubrimientos s/n, 41092, Sevilla, Spain*

7 ^c *Laboratory of Engineering for Energy and Environmental Sustainability, Universidad de*
8 *Sevilla, Camino de los Descubrimientos s/n, 41092, Sevilla, Spain*

9 ^d *Faculty of Engineering, University of Porto, Portugal*

10

11 **Keywords:**

12 Railway track geometry; Ballast settlement modelling; Subgrade settlement modelling;
13 Railway track-ground settlement; Vehicle-track interaction; Railway track-ground non-
14 linearity

15

16 **Abstract**

17 Railway tracks undergo plastic settlement when subject to repeated train loading. This
18 occurs differentially along the track rather than in a uniform manner, and the profile is a key
19 parameter when scheduling track maintenance operations. Therefore this paper presents a
20 novel numerical approach to predict track irregularity evolution. The model combines
21 empirical settlement laws with finite element theory, where the track-ground structure is
22 modelled explicitly, and multi-body train-track interaction is considered. The stresses
23 induced by rolling stock are solved using a hybrid frequency-wavenumber and time-space
24 approach, considering non-linear track-soil material behaviour. It has several novelties: 1)
25 after every load passage, the track profile is updated before applying the next load, meaning
26 the train-track interaction is constantly evolving; 2) new empirical settlement laws are
27 derived that account for evolving train-track forces and track profiles; 3) fully 3D stress fields
28 in the track and ground are considered. First the model is described, before validating its
29 prediction of track geometry evolution, captured from track recording vehicles. Next, it's
30 used to show that modelling error is introduced if the geometry isn't updated frequently
31 (e.g. after every load passage). Finally, a parametric study shows track subgrade material
32 properties have a marked effect on track settlement.

33

34 **1. Introduction**

35 Under every axle passage, railway tracks experience a small amount of permanent
36 deformation (Li et al., 2015). Due to dynamic loading and varying track support conditions
37 along the track, successive axle passage lead to long-term non-uniform (aka differential)
38 settlement (Fröhling, 1998). These changes in track level over a given distance define the
39 track geometry. Track geometry can deteriorate rapidly once differential settlement starts

40 to occur, because degradation induces higher train-track dynamic interaction forces, thus
41 leading to further track settlement.

42 Track quality measurement is typically performed by a track recording car and a variety of
43 metrics can be used to define a track quality index (TQI) (Yan and Corman, 2020). Different
44 countries have developed and implemented TQI's in different ways, however, the standard
45 deviation (SD) of vertical track geometry over a given distance is widely used (Neuhold et al.,
46 2020). The higher the SD value, the lower quality of the track. When the SD of the track
47 geometry reaches a threshold limit value, maintenance action is required.

48 Tamping is a common track maintenance activity used to correct vertical track geometry
49 faults for wavelengths within a certain range (for example, between 3-25 m (Esveld, 2001),
50 or 3-35m (Network Rail, 2015)). When the variation in geometry exceeds a threshold limit,
51 corrective tamping restores it to an acceptable value, thus helping to extend the track life
52 between full track reconstructions. Rather than wait until a SD threshold value is reached
53 and then perform emergency maintenance, common practise is to attempt to predict the
54 future date when maintenance is required. Then it can be planned, resulting in minimal line
55 disruption. To predict these maintenance schedule dates, most commonly, on existing lines,
56 historical changes in track geometry at a given location are extrapolated into the future to
57 determine degradation (Lee et al., 2020). However, this approach is challenging for cases
58 where significant changes are made to the track or rolling stock. In such situations,
59 historical data is unlikely to be representative of future behaviour. For example:

- 60 • New track construction. In this case historical geometry records don't exist.
- 61 • The changing of rolling stock characteristics. For example, raising line speed,
62 increased freight-passenger traffic ratios, and deploying new rolling stock. In these
63 cases, the changes in vehicle-track dynamics will lead to different dynamic stress
64 fields in the track. Therefore the settlement rate may be different from historical.
- 65 • The changing of track characteristics. For example, new track designs, adding new
66 track components, and renewing the track/subgrade. In these cases the dynamic
67 stiffness and strength characteristics of the track may lead to settlement rates that
68 differ from historical.

69 There are two main modelling approaches to predict track settlement: constitutive and
70 empirical. Models based on constitutive relationships attempt to simulate the physical
71 behaviour of materials, using for example, yield criteria, flow rules and hardening rules
72 (Dahlberg, 2001; Indraratna et al., 2012; Suiker and de Borst, 2003). These can be
73 implemented within a finite element model, however the discrete element method (DEM)
74 can also be used to simulate local deformations and heterogeneous particle displacements
75 (Guo et al., 2020; Saussine et al., 2006). Considering the FE approach, an implementation in
76 3D made in a commercial FE software combining with an elasto-plastic constitutive model
77 was presented by (Shih et al., 2019) to calculate differential settlement in ballasted tracks.
78 A constitutive model integrated with an iterative procedure was developed in (Li et al.,
79 2016) to compute differential track settlement accounting for longitudinal variations in load
80 and track characteristics. However, a challenge with such constitutive models is that they
81 often require input parameters related to the ballast and subgrade that are difficult to
82 measure/quantify. Further, they are often computationally intensive, thus making the
83 prediction of long-term differential settlement due to dynamic train loads challenging (Chen
84 and McDowell, 2016; Shan et al., 2017).

85 An alternative approach for settlement modelling is to use empirical settlement equations.
86 Several models, see for example (Indraratna and Nimbalkar, 2013; ORE, 1970; Sato, 1995;
87 Shenton, 1985), have been developed for the prediction of ballast settlement under cyclic
88 loading. These typically identify empirical parameters using cyclic triaxial test data,
89 reduced-scale models (Menan Hasnayn et al., 2017; Yu et al., 2019), or in situ
90 measurements. Similarly, empirical parameters for the prediction of subgrade settlement
91 have been obtained by conducting laboratory tests on different soil conditions to investigate
92 plastic deformation under repeated load applications (Li, 1994; Li and Selig, 1996; Liu and
93 Xiao, 2010). Compared with constitutive modelling, the published results achieved using
94 empirical models are similar in accuracy to constitutive ones, however only depend upon a
95 minimal number of input parameters that are usually relatively straightforward to
96 determine (Ramos et al., 2020).

97 However, one drawback of the existing empirical models presented in the literature is that
98 they assume the ballast and subgrade materials are subject to cyclic loads of equivalent
99 magnitudes. This is not the case in real life, because track irregularities evolve with each
100 axle passage. Therefore, for each subsequent passage, the train-track dynamic interaction
101 forces, the distribution of stresses within the track layers, and ultimately the induced
102 settlement is different. Further, in real life, most tracks are subject to mixed types of rolling
103 stock (e.g. freight and passenger), running together on a timetable. In such situations,
104 where the simulation of multiple vehicles is required, it is challenging to use the current
105 forms of empirical settlement equations, because the dynamic loads are different for each
106 vehicle.

107 A key input to constitutive and empirical settlement models are stresses induced in both
108 ballast and subgrade. These stresses are often calculated using a numerical mode. One
109 example of using numerical modelling combined with empirical settlement laws is
110 presented by Sayeed and Shahin (Sayeed and Shahin, 2018). Settlement is calculated in
111 both the ballast and subgrade, using a 3D finite element approach to compute the
112 deviatoric stress, considering the effect of a moving dynamic train load. However, the track
113 geometry profile is not updated after subsequent axle passages. Instead an empirical
114 settlement law is used to extrapolate its change, based upon the results of the initial train
115 passage. This is a drawback because changes in the track geometry influence the train-track
116 interaction forces, which are closely linked to track unevenness (Burrow et al., 2017).
117 Therefore, under certain circumstances, this approach may under-predict the deterioration
118 of track geometry.

119 Alternatively, methodologies have been proposed to predict differential track settlement
120 considering train-track dynamic interaction, accounting for the evolution of track geometry
121 irregularities. For example, Zuada Coelho (Zuada Coelho et al., 2021) introduces a
122 methodology to predict track settlement considering the effect of traffic changes, but at the
123 network scale. The corresponding forces due to the dynamic deformation during train
124 operation are computed, however not every axle passage is considered. Alternatively, Guo
125 and Zhai (Guo and Zhai, 2018) apply an iterative method to estimate the long-term
126 settlement of ballastless track, considering the evolution of differential settlement in the
127 subgrade. An empirical model for subgrade settlement is proposed. The deviatoric stress
128 exerted on the surface of subgrade is combined with an exponential attenuation equation.
129 Further, Nielsen and Li (Nielsen and Li, 2018) propose a numerical method based on an
130 iterative approach combined with an empirical model to predict the deterioration of track

131 geometry due to differential settlement. The foundation is modelled using a beam-on-
132 elastic-foundation approach (i.e. springs and dampers). Grossoni (Grossoni et al., 2021)
133 presents a semi-analytical approach based on an investigation of material behaviour under
134 cyclic loading combined with a train-track interaction model, that allows for the estimation
135 of differential ballast settlement due to evolving track roughness. Plastic settlement is
136 modelled at each loading cycle as a function of the vertical stress.

137 A common strategy in the aforementioned approaches is to model the track using springs
138 and dashpots, and then solve in the time domain. Although this provides some advantages,
139 it doesn't allow for the calculation of 3D dynamic stress fields in the track and the subgrade.
140 Deviatoric stress is one of the most influential parameters on permanent deformation
141 (Indraratna et al., 2010; Li and Selig, 1996) and therefore is closely linked to differential
142 settlement. Although deviatoric stresses can be calculated in 2D, which is acceptable for
143 certain engineering applications, when considering wave propagation problems, 3D
144 modelling provides highest accuracy (Arcos et al., 2021; Xu et al., 2015). Therefore for
145 railway applications that require accurate stress wave simulation (e.g. ground-borne
146 vibration and critical velocity) the calculation of 3D fields has become standard practise.

147 In an attempt to address these challenges, this paper first proposes several recommended
148 characteristics to calculate differential railway track settlements. Then a practical
149 implementation of these characteristics is shown by developing a novel numerical approach
150 capable of considering 3D stress fields, evolving track geometry and train-track interaction
151 forces. The model is based on a FEM-PML (Finite Element Method with Perfectly Matched
152 Layers) approach, solved in a hybrid manner, across both frequency-wavenumber and time-
153 space domains. Train-track interaction, vehicle dynamics and 3D stress field propagation
154 are modelled explicitly. After every load passage, the vertical track irregularities along the
155 track length are updated, and the train-track dynamic interaction force and the distribution
156 of dynamic stress are recalculated as a consequence. By taking advantage of a mixed
157 frequency-wavenumber, time-space domain approach, the computational efficiency of the
158 implementation is high, and thus allows the differential settlement to be updated after
159 every train axle passage, even when using solid elements to capture 3D stress fields.
160 Further, to maximise accuracy for heavy and fast moving axle loads, the non-linear stiffness
161 characteristics of both the granular track and subgrade materials are accounted for.

162

163 **2. Characteristics of a differential settlement prediction model**

164 Long-term track geometry changes are important for predicting future maintenance
165 schedules, particularly automated tamping. Therefore any numerical model should be able
166 to predict differential settlement for the wavelength range over which tamping is effective,
167 and the timeline until the next tamping cycle should be scheduled. The forecasting of long-
168 term track settlement is challenging, involving numerous variables such as train-track
169 interaction, an evolving track profile and non-linear soil behaviour. Further, when
170 considering a large number of load passages, small inaccuracies at each iteration are
171 magnified and can greatly affect the final predicted settlement. Thus, for a numerical
172 approach attempting to do this, the following are important to consider:

173 1. Calculation of 3D stress fields in the track and ground. This is important because
174 deviatoric stress is an influential parameter on settlement

175 2. Calculation of train-track interaction forces. The dynamic forces caused by the interaction
176 between track geometry irregularities and rolling stock are a key source of differential
177 settlement on plain line. The degradation of track geometry results in higher train-track
178 dynamic interaction forces which effect on the distribution of the stresses, and thus further
179 track settlement (Bian et al., 2015).

180 3. Simulation of the evolution of train-track interaction forces. Track geometry degrades
181 after train passages, meaning future train passages are likely to generate different
182 deviatoric stresses and differential settlement, compared to previous trains. This is
183 particularly important when modelling a line with mixed rolling stock.

184 4. Simulation of the evolution of track-subgrade settlement laws. Track settlement rate is
185 dependent upon the settlements from ballast and subgrade layers induced by previous axle
186 loads. Considering the dynamic forces exerted on the track change as the track geometry
187 evolves, the settlement relationship should consider this.

188 These characteristics can be achieved using different modelling approaches. For example, a
189 direct approach can be used where non-linear soil behaviour is modelled directly.
190 Alternatively, an indirect approach can be used, where the ground stress fields are
191 estimated using an equivalent linear approach, and then the stress fields used to compute
192 settlement using empirical laws. Although the first approach is more exact from the
193 theoretical viewpoint, its application requires significant computational resources and the
194 estimation of many input parameters to accurately define non-linear soil behaviour.
195 Therefore, with the aim of acting as a practical tool for engineering purposes, the second
196 strategy is preferred.

197 **3. Numerical modelling overview**

198 A variety of numerical simulation approaches can be used to meet the characteristics
199 mentioned above, however the criteria imply that the problem should be modelled in 3D,
200 consider vehicle dynamics and train-track interaction, and be able to update the track
201 geometry after an arbitrary number of loads with arbitrary magnitude. To achieve these
202 objectives, this paper proposes a novel, 2-step coupled modelling strategy, solved in a
203 hybrid manner, across both time-space and frequency-wavenumber domains. The two
204 primary steps are as shown in Figure 1:

205 **Step A:** Calculates the 3D elastodynamic response of the track-ground system in the
206 frequency-wavenumber domain. The geo-static stresses and the moving load transfer
207 function that accounts for soil stiffness non-linearity are computed. The 3D stress fields,
208 which include quasi-static and dynamic components, are then calculated in terms of
209 wavenumber and frequency. This part is only computed once for each moving speed of
210 vehicle being considered. Also, the matrices for train and track compliance required for
211 train-track dynamic interaction are computed. These various pre-calculated fields then
212 allow Step B to be computed in an efficient manner for every axle passage.

213 **Step B:** Calculates the differential track settlement using a combination of time and
214 frequency domain methods. The train-track dynamic interaction force, the deviator stress
215 and the settlement in the track and ground are calculated. The total deviator stress includes
216 quasi-static stress, dynamic stress and geo-static stress. After every load passage the track
217 irregularity profile is updated and thus the new train-track dynamic force is recalculated.

218 These steps are repeated until the defined number of load cycles or threshold geometry
 219 criteria is reached.
 220

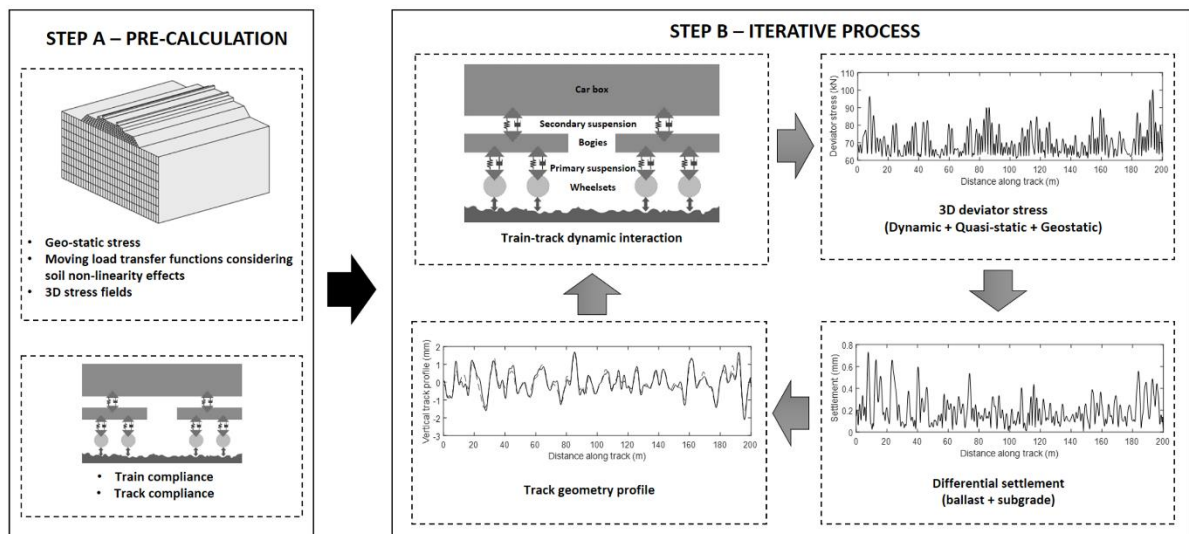


Figure 1. Model overview

221
 222
 223

4. Numerical model description

4.1.1. General formulation

226 The wavenumber finite element method (aka two-and-a-half dimension approach) is a
 227 computationally efficient method for the solution of three-dimensional domains. Two
 228 dimensions are solved via finite element theory while the third is solved analytically. It is
 229 therefore well-suited for 3D structures that can be approximated as having invariant
 230 geometry and material properties in one direction (e.g. railways, highways and tunnels). An
 231 example discretisation of the track-ground structure using the developed mesh generator is
 232 illustrated in Figure 2. This cross-section remains invariant in the longitudinal direction of
 233 the track, however the loading is 3D and the track-ground response is calculated in 3D. The
 234 interactions between different interfaces/layers are modelled accounting for the continuity
 235 of displacements and equilibrium of stresses along each subdomain interface (François et
 236 al., 2010).

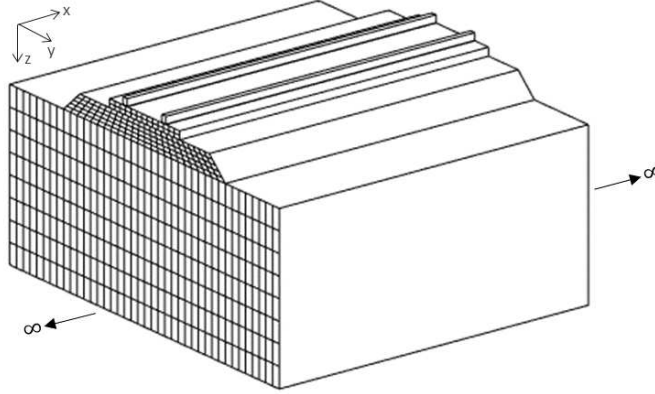


Figure 2. Infinite and invariant structure in the x direction

237

238

239 Assuming the structure is linear and elastic, the equations of motion can be solved in the
 240 wavenumber-frequency domain. A double Fourier transform is used to transform all
 241 variables into the wavenumber-frequency domain in terms of the moving direction of the
 242 train (x direction) and time (t).

243 Following a general finite element formulation, the following equilibrium equation
 244 represents any point in the 3D domain:

$$\int_V \delta \varepsilon \sigma dV + \int_V \delta u \rho \frac{\partial^2 u_i(x, t)}{\partial t^2} dV = \int_S \delta u p dS \quad (1)$$

245 where $\delta \varepsilon$ is the virtual strain field; σ is the stress field; δu is the virtual displacement field; u
 246 is the displacement field; ρ is the mass density; and p is the applied load.

247 Eq. (1) can be rewritten in terms of nodal variables because the untransformed domain
 248 cross-section is discretised into finite elements. Then, considering Parseval's theorem
 249 (Hardy and Littlewood, n.d.), the concept of virtual work is applied to the transform domain.
 250 The functions of the Fourier images of x and t are defined as wavenumber and frequency
 251 denoted by k_x and ω , respectively. Therefore, in the transformed domain, the virtual work
 252 of the internal stresses and inertial forces is:

$$\int_V \delta \varepsilon \sigma dV = \int_{k_x} \delta u_n^T(-k_x, \omega) \int_z \int_y B^T(-k_x) D B(k_x) dy dz u_n(k_x, \omega) dk_x \quad (2)$$

$$\int_V \delta u \rho \frac{\partial^2 u(x, t)}{\partial t^2} dV = -\omega^2 \int_{k_x} \delta u_n^T(-k_x, \omega) \int_z \int_y N^T \rho N dy dz u_n(k_x, \omega) dk_x \quad (3)$$

253 where B is the matrix containing the derivatives of the finite element shape functions; D is
 254 the elasticity matrix; N is the shape function matrix; and u_n is the nodal displacement vector
 255 in the transformed domain.

256 Taking advantage of the finite element discretisation on the YZ plane and considering a
 257 coordinate 'S' parallel to the edge the element where traction is applied, the virtual work
 258 induced by the load is:

$$\int_S \delta u p dS = \int_{k_x} \delta u_n^T(-k_x, \omega) \int_S N^T p(k_x, \omega) ds dk_x = \int_{k_x} \delta u_n^T(-k_x) p_n(k_x, \omega) dk_x \quad (4)$$

259 Then, substituting Eqs. (2)-(4) into Eq. (1), the equilibrium of each finite element in the YZ
 260 plane is:

$$\left(\int_z \int_y B^T(-k_x)DB(k_x) dy dz - \omega^2 \int_z \int_y N^T \rho N dy dz \right) u_n(k_x, \omega) = p_n(k_x, \omega) \quad (5)$$

261 Considering classic finite element notation, the stiffness $[K]$ and mass $[M]$ matrices are:

$$[K] = \int_z \int_y B^T(-k_x)DB(k_x) dy dz \quad (6)$$

$$[M] = \int_z \int_y N^T \rho N dy dz \quad (7)$$

262 The matrix $[B]$ is derived from the differential operator matrix $[L]$ and the shape function
 263 matrix $[N]$. The longitudinal direction x is transformed into the wavenumber domain,
 264 meaning the derivatives in direction x , represented by k_x , are computed analytically.

$$[L] = \begin{bmatrix} ik_x & 0 & 0 & \frac{\partial}{\partial y} & 0 & \frac{\partial}{\partial z} \\ 0 & \frac{\partial}{\partial y} & 0 & ik_x & \frac{\partial}{\partial z} & 0 \\ 0 & 0 & \frac{\partial}{\partial z} & 0 & \frac{\partial}{\partial y} & ik_x \end{bmatrix}^T \quad (8)$$

265 In terms of damping, a hysteretic damping model is implemented in the frequency domain
 266 method via a complex stiffness. The stiffness matrix $[K]$ can be divided into several sub-
 267 matrices, independent of the wavenumber (k_x) and frequency (ω) to improve the
 268 computation effort. After separating the numerical and analytical derivatives, Eq. (5) is
 269 defined as:

$$([K_1] + ik_x[K_2] + k_x^2[K_3] - \omega^2[M])\{u_n\} = \{p_n\} \quad (9)$$

270 Assuming the system is symmetrical along its centreline, discretisation can be implemented
 271 considering only half of the domain. After solving the global system of equations, the
 272 displacements in the transformed domain require a double inverse Fourier transform in
 273 order to obtain a solution in the space-time domain.

274 4.1.2. Sleeper elements

275 The 2.5D method assumes invariant geometry in the direction of train passage. Although
 276 the approximation of discrete sleepers using an equivalent continuous formulation gives
 277 acceptable results for the frequency range of study (Knothe and Wu, 1998), to maximise
 278 accuracy an anisotropic constitutive material model is used to account for discrepancies in
 279 bending stiffness.

280 To do so, the approach proposed by Alves Costa et al. (Alves Costa et al., 2010) and
 281 Karlstrom and Bostrom (Karlström and Boström, 2006) is used. The sleepers are modelled
 282 as continuous and orthotropic elements, where the physical properties of the sleepers are
 283 used in the cross-section. To do so, in the longitudinal plane, the stiffness is set as close to
 284 zero. Therefore, the elasticity matrix $[D]_{sleeper}^{-1}$ used to simulate the sleeper elements is:

$$[D]_{sleeper}^{-1} = \begin{bmatrix} \frac{1}{E_x} & -\frac{\nu_{xk}}{E_k} & -\frac{\nu_{xk}}{E_k} & 0 & 0 & 0 \\ \frac{\nu_{xk}}{E_x} & \frac{1}{E_x} & -\frac{\nu_{kk}}{E_k} & 0 & 0 & 0 \\ -\frac{\nu_{xk}}{E_x} & -\frac{\nu_{kk}}{E_k} & \frac{1}{E_x} & 0 & 0 & 0 \\ 0 & 0 & 0 & \frac{1}{G_{xk}} & 0 & 0 \\ 0 & 0 & 0 & 0 & \frac{1}{G_{kk}} & 0 \\ 0 & 0 & 0 & 0 & 0 & \frac{1}{G_{xk}} \end{bmatrix} \quad (10)$$

$$G_{kk} = \frac{E_k}{2(1+\nu_{kk})} \quad (11)$$

285 where E_k is the Young's modulus of the sleepers in the isotropic YZ plane; ν_{kk} is Poisson's
 286 ratio of the sleeper in the isotropic YZ plane; G_{kk} is the shear modulus in the isotropic YZ
 287 plane; E_x is Young's modulus of the sleepers in the track direction; ν_{xk} is Poisson's ratio of
 288 the sleeper in the track direction; and G_{xk} is the shear modulus in the track direction.

289 4.1.3. Rail and rail pad elements

290 The rails are Euler-Bernoulli beams supported by rail pads which are modelled as springs
 291 and dampers connected to the sleeper, as illustrated in Figure 3. Since the beam is defined
 292 in the longitudinal direction of the track, the system of equations can be analytically
 293 computed in the frequency-wavenumber domain without numerical discretisation and
 294 integration, using:

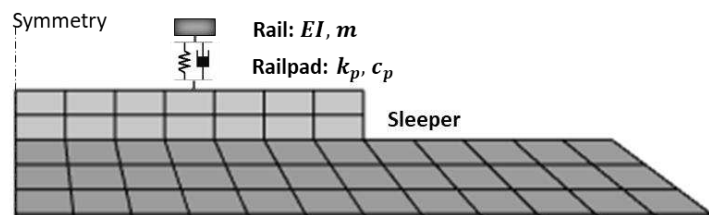
$$([K_1^{railpad}] + k_x^4 [K_2^{rail}] - \omega^2 [M^{rail}]) \{u_n\} = \{p_n\} \quad (12)$$

$$[K_1^{railpad}] = \begin{bmatrix} k_p^* & -k_p^* \\ -k_p^* & k_p^* \end{bmatrix} \quad (13)$$

$$[K_2^{rail}] = \begin{bmatrix} EI_r & 0 \\ 0 & 0 \end{bmatrix} \quad (14)$$

$$[M^{rail}] = \begin{bmatrix} m_r & 0 \\ 0 & 0 \end{bmatrix} \quad (15)$$

295 where EI_r is the bending stiffness of the rail; m_r is the mass per unit length of the rail; and
 296 k_p^* is the complex stiffness of the rail pad taking rail pad's damping into account. In this
 297 case, $k_p^* = k_p + i\omega c_p$, where k_p is the stiffness of the rail pad and c_p is the viscous damping
 298 factor of the rail pad; $\{u_n\}$ is the vectors that collect the vertical displacements of the rail
 299 and rail pad or sleeper components.



300
301 Figure 3. Rail-sleeper connection

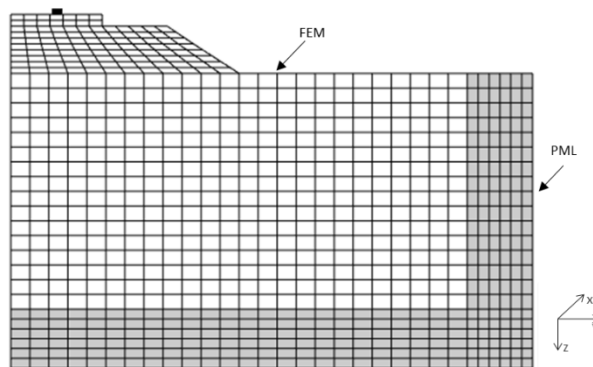
302 Taking into account the global system of equations, the rail pad stiffness in $[K_1^{railpad}]$ and
 303 the rail mass per unit length in $[M^{rail}]$ can be assembled with the matrices $[K_1]$ and $[M]$ in
 304 Eq. (9) respectively. The imaginary part of the matrix $[K_1^{railpad}]$ is collected in order to form
 305 a damping matrix defined as $[C]$. After assembling the element stiffness matrices, the
 306 generalised 2.5D finite element equilibrium equation is given by:

$$([K_1] + ik_x[K_2] + k_x^2[K_3] + k_x^4[K_4] + i\omega[C] - \omega^2[M])\{u_n(k_x, \omega)\} = \{p_n(k_x, \omega)\} \quad (16)$$

307 4.1.4. Perfectly matched layers

308 The excitation induced by the passage of the train can be decomposed into two main
 309 components: (i) quasi-static load, resulting from the weight of the train; (ii) dynamic load,
 310 due to the dynamic interaction between the wheel and the rail. In comparison to the quasi-
 311 static load (at speeds below critical velocity), dynamic loading generates propagating waves
 312 in the ground and thus high performance absorbing boundaries are needed to prevent
 313 domain boundary reflections. Perfectly matched layers consist of layers of elements with
 314 identical material properties to the region of the domain they bound. Each sub-layer within
 315 the PML domain acts to dampen outgoing waves, and therefore the combined effect of
 316 multiple sub-layers is an efficient way to maximise performance. An example setup is
 317 shown in Figure 4, where the cross section of the 2.5D model is discretised into finite
 318 elements and bounded by adding external layers that are formed by PML's. The waves
 319 impinging the boundary between each domain are described by the 2.5D FEM and the 2.5D
 320 PML. The PML mesh is 1m thick and divided into 6 sub-layers.

321



322

323

Figure 4. Representative half-track model with PML

324 The x coordinate is transformed to the wavenumber domain, and thus only the coordinates
 325 y and z are stretched by the PML in the complex domain. To allow for the absorption of
 326 waves inside the PML domain, the same differential equations used in the FEM domain are
 327 modified by considering stretched coordinates \tilde{y} and \tilde{z} :

$$\tilde{y} = \int_0^y \lambda_y(y) dy \quad (17)$$

$$\tilde{z} = \int_0^z \lambda_z(z) dz \quad (18)$$

328 The non-zero complex valued stretching functions in the y direction (λ_y) and in the z
 329 direction (λ_z) are defined using functions:

$$\lambda_y(y) = \frac{2\pi y}{|k| H_y} - i \frac{k_0}{k} \left(\frac{y}{H_y} \right)^2 \quad (19)$$

$$\lambda_z(z) = \frac{2\pi z}{|k| H_z} - i \frac{k_0}{k} \left(\frac{z}{H_z} \right)^2 \quad (20)$$

330 where k_0 is a constant (e.g. Lopes et al. (Lopes et al., 2014) recommend $k_0 = 20$); H_y is the
331 thickness of the PML in the y direction; H_z is the thickness of the PML in z direction; and k is
332 the effective wavenumber for waves propagating along the cross-section, which is given by:

$$k = \sqrt{\left(\frac{\omega}{C_s} \right)^2 - k_x^2} \quad (21)$$

333 where C_s is the velocity of shear wave.

334 The coordinates y and z in the equilibrium equation are replaced by \tilde{y} and \tilde{z} respectively.

335 The partial derivatives with respect to \tilde{y} and \tilde{z} are expressed using the following
336 relationships:

$$\frac{\partial}{\partial \tilde{y}} = \frac{1}{\lambda_y(y)} \frac{\partial}{\partial y} \quad (22)$$

$$\frac{\partial}{\partial \tilde{z}} = \frac{1}{\lambda_z(z)} \frac{\partial}{\partial z} \quad (23)$$

337 Since the solution within the PML domain satisfies the same differential equation as in the
338 2.5D domain, the stiffness and mass matrices for the PML region can be derived from Eq. (6)
339 and Eq. (7) respectively. The differential operator $[L^*]$ is given by:

$$[L^*] = \begin{bmatrix} ik_x & 0 & 0 & \frac{1}{\lambda_y(y)} \frac{\partial}{\partial y} & 0 & \frac{1}{\lambda_z(z)} \frac{\partial}{\partial z} \\ 0 & \frac{1}{\lambda_y(y)} \frac{\partial}{\partial y} & 0 & ik_x & \frac{1}{\lambda_z(z)} \frac{\partial}{\partial z} & 0 \\ 0 & 0 & \frac{1}{\lambda_z(z)} \frac{\partial}{\partial z} & 0 & \frac{1}{\lambda_y(y)} \frac{\partial}{\partial y} & ik_x \end{bmatrix}^T \quad (24)$$

340 Due to the frequency dependence of the stretching functions inside the PML domain, the
341 equilibrium condition after assembling the equations of each individual element is:

$$\left([K_{FEM}^{global}(k_x)] + [K_{PML}^{global}(k_x, \omega)] - \omega^2 ([M_{FEM}^{global}] + [M_{PML}^{global}(k_x, \omega)]) \right) \{u_n(k_x, \omega)\} = \{p_n(k_x, \omega)\} \quad (25)$$

342 where $[K_{FEM}^{global}]$ and $[K_{PML}^{global}]$ are the global stiffness matrices of the FEM and PML
343 domains respectively, and $[M_{FEM}^{global}]$ and $[M_{PML}^{global}]$ are the mass matrices of the FEM and
344 PML domains respectively.

345 4.1.5. Soil stiffness non-linearity

346 When train speed is high and/or axle loads are heavy, large strains can be induced in the
347 soil, and thus the probability of non-linear stiffness behaviour increases (Dong et al., 2019;
348 Shih et al., 2017). This behaviour effects stress wave generation and propagation, and thus
349 settlement, meaning it is important to capture.

350 The typical stress-strain behaviour of track and ground during cyclic loading can be
351 described by a nonlinear hysteretic loop (Hardin and Drnevich, 1972). This causes the soil
352 stiffness to decrease and the damping ratio to increase as strain increases. To assess non-
353 linear behaviour in the frequency domain while minimising computational demand, an

354 equivalent linear approach is used. The shear modulus reduction curve and the damping
355 ratio are based on an empirical equation proposed by (Ishibashi and Zhang, 1993) which
356 requires cyclic shear strain amplitude (γ_{eff} in this case), mean effective confining pressure
357 and the soil's plasticity index as inputs. Regarding the embankment material, the
358 relationship proposed by (Rollins et al., 2020a) is used.

359 An iterative procedure based on the effective octahedral shear strain is used to update the
360 properties of each element until agreement between the material properties and strain-
361 adjusted properties is achieved. This implementation can be summarised in the following
362 steps:

- 363 1. Start calculation assuming low strain properties for all elements
- 364 2. Use Eq. (26) to compute the effective octahedral shear strain from strain time histories
365 and select the maximum value for each element
- 366 3. Use the maximum values of the effective octahedral shear strain with stiffness-strain
367 relationship and damping-strain relationship curves (e.g. Figure 9) to compute new
368 equivalent linear values, and update the stiffness and the damping of each element in
369 anticipation of the next iteration. Note that for unbounded soil regions, PML elements
370 are updated using the properties from the closest elements within the intersecting FE
371 domain
- 372 4. Repeat steps 2-3 until the differences between both the shear modulus and damping in
373 successive iterations fall below 3% for all elements (Alves Costa et al., 2010)

374 As the model is used to calculate 3D stress fields, the effective octahedral shear strain is
375 computed as:

$$\gamma_{eff} = \alpha \frac{1}{3} \sqrt{(\varepsilon_x - \varepsilon_y)^2 + (\varepsilon_x - \varepsilon_z)^2 + (\varepsilon_y - \varepsilon_z)^2 + 6(\gamma_{xy}^2 + \gamma_{xz}^2 + \gamma_{yz}^2)} \quad (26)$$

376 where α is 0.65 (as typically used in seismic analysis); ε_x , ε_y and ε_z are the strains in three
377 directions; and γ_{xy} , γ_{xz} and γ_{yz} are the corresponding shear strains. The non-linear
378 calculation procedure is performed during Step A and the strain-adjusted material
379 properties are passed to Step B for settlement calculation.

380

381 **4.2. Train-track interaction**

382 Accurately simulating vehicle dynamics and train-track interaction is vital for differential
383 settlement prediction. This is because it is the interaction between wheel and rail that
384 induces differing dynamic forces along the track, that create track-ground stresses, which in
385 turn govern settlement. To simulate this, vehicle-track interaction is solved using a
386 compliance procedure formulated in a moving frame of reference, subject to a moving train
387 (Colaço et al., 2016; Costa et al., 2012). As vertical differential settlement is the parameter
388 under investigation, only vertical dynamics are considered.

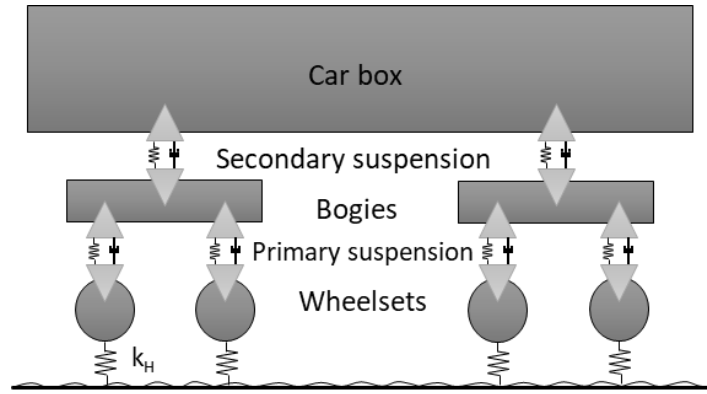
389 **4.2.1. Vehicle model**

390 The equilibrium equations for the vehicle and the track are formulated separately. Then the
391 interaction forces between these two structural systems are calculated respecting
392 equilibrium conditions and displacement compatibility at the connecting points. Assuming

393 perfect contact between train and track, any temporal instant for all connection points
 394 between the wheel and the rail is fulfilled by:

$$u_{c,i} = u_r \left(t = \frac{x-a_i}{v_0} \right) + u_{irr} \left(t + \frac{a_i}{v_0} \right) + \frac{P_{dyn,i}(t)}{k_H} \quad (27)$$

395 where u_r is the vertical displacement of the rail; $u_{c,i}$ is the vertical displacement at the
 396 contact point i ; a_i is the location of the contact point i ; v_0 is the moving speed of the
 397 vehicle; t is the time; u_{irr} is the vertical track irregularity; $P_{dyn,i}$ is the dynamic interaction
 398 load at the contact point i ; and k_H is the Hertzian stiffness.



399
 400 *Figure 5. Multi-body vehicle model*

401 A rigid multi-body vehicle model with two levels of suspension, as proposed by Zhai and Cai
 402 (Zhai and Cai, 1997) is considered (Figure 5). Since the analysis is performed in the
 403 frequency domain, Eq. (27) can be formed in the frequency domain using the
 404 transformation of the unevenness track for that domain. Therefore, the dynamic
 405 interaction forces in the frequency domain are:

$$\{F_{dyn}(\Omega)\} = -([V] + [V^H] + [T])^{-1} \{\Delta u(\Omega)\} \quad (28)$$

$$\{\Delta u(\Omega)\} = \delta u \{b(\Omega)\} \quad (29)$$

$$b(\Omega)_i = e^{i\frac{2\pi}{\lambda}a_i} \quad (30)$$

$$T(\Omega) = \frac{1}{2\pi} \int_{-\infty}^{+\infty} u_c^G(k_x, \omega) dk_x \quad (31)$$

$$V^H = \frac{1}{k_H} \quad (32)$$

$$V(\Omega) = [Z]([K^v] - \Omega^2[M^v])^{-1}[Z]^T \quad (33)$$

406 where Ω is the driving frequency, defined by $\Omega = \frac{2\pi}{\lambda} v_0$; T is the flexibility term of the track
 407 compliance; V is the flexibility term of the vehicle compliance; V^H is the contact flexibility
 408 matrix; Z is a constant matrix, M^v is the vehicle mass matrix and K^v is the vehicle stiffness.

409 The mass and stiffness matrices of the vehicle system with primary and secondary
 410 suspensions are given in the Appendix.

411 Regarding the Hertzian stiffness, since the dynamic portion of the contact force is typically
412 substantially less than the static action (weight of the train per wheel), the contact stiffness
413 can be linearised considering only the portion of the force P corresponding to the
414 distribution of the weight of the train per wheel (Sheng et al., 2003; Wu and Thompson,
415 2001). Therefore, a linearization procedure can be adopted, in which only the dead load
416 transmitted by the wheelset is taken into account (Kouroussis et al., 2014). The linearised
417 (Hertzian) contact stiffness is defined as:

$$k_H = \frac{3}{2G} P_0^{1/3} \quad (34)$$

418 where P_0 is the static load transmitted by the wheel to the rail; and G is the contact constant
419 depending on the radius and geometry of the wheel, and rail bearing surface.

420 **4.2.2. Track irregularities**

421 The geometric irregularity of the track can be defined using either a synthetic profile or from
422 data gathered by an in-service measurement vehicle. Track irregularities can be described
423 using power spectral density (PSD) as a function of spatial frequency, of which there are
424 various formulations. The formulation used in this work is based on the Federal Railway
425 Administration (FRA) which divides the track into different classes for the quantification of
426 track unevenness (Federal Railroad Administration, 1980).

427 In contrast to artificial track irregularities, measured irregularity profiles can also be used for
428 simulating dynamic excitation. The raw signals from measurement are band-pass filtered to
429 obtain signal wavelengths within the interested range. In addition, the signals are
430 proceeded using a transformation from the space domain into the spatial frequency
431 domain, since the analysis is conducted in the frequency domain. Instead of using the
432 Fourier Transform, it is necessary to take into account the discrete nature of the digital
433 signals. Therefore, a Discrete Fourier Transform is applied (Cooley and Tukey, 2019) to deal
434 with the domain transformation process of the measured track irregularity profile.

435

436 **4.3. Permanent strain and settlement models**

437 **4.3.1. Ballast settlement**

438 The ballast settlement model is inspired by the ORE-type formulation (ORE, 1970) which
439 depends upon the number of loading cycles, deviator stress and ballast porosity. The
440 empirical constants are adjusted to improve the fit with the experimental data generated by
441 (Abadi et al., 2016). Figure 6 shows curve fits from the proposed equation and the
442 experimental data in the settlement rate, against the logarithm of the number of load
443 cycles. It should be noted that the permanent strain during the first cycles is removed to
444 avoid any effects due to the initial rapid rearrangement of ballast particles during lab
445 testing. The proposed equation shows a strong fit with the experimental data.

446 A key advantage of using an iterative modelling approach is that the differential settlement
447 and track profile can be updated after every load passage. However, this requires that the
448 deviatoric stress must also be recalculated after every passage. Further, the equation must
449 be able to compute settlement for varying scenarios, including:

- 450 1. The case of newly constructed or renewed/tamped track, where the ballast has only
 451 experienced minimal loading
 452 2. The case of existing ballast, where the ballast has previously been compacted under
 453 a large volume of traffic

454 Considering these factors and the need to regularly update the track profile, an alternative
 455 form of the ORE settlement equation is required, that is able to account for the settlement
 456 of previous axle passages in its calculation. Therefore a modified permanent strain
 457 equation, computed at every iterative step is proposed:

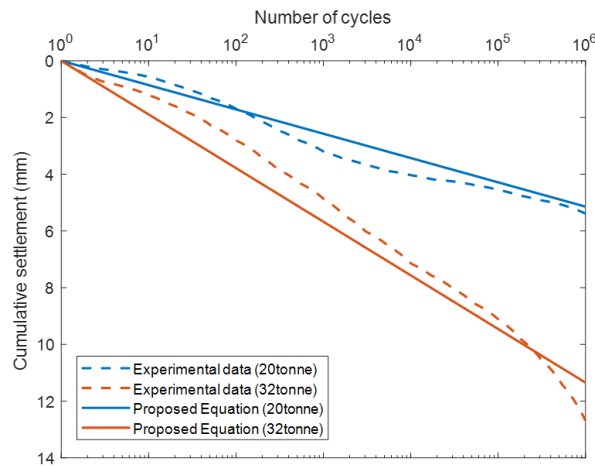
458

$$\Delta\varepsilon_{p,b,i} = 0.375(\sigma_{d,b,i})^2 \times \left[(1 + 0.4 \log_{10}((dN \cdot i) + N_{lb})) - (1 + 0.4 \log_{10}((dN \cdot (i - 1)) + N_{lb})) \right] \quad (35)$$

The corresponding settlement is then:

$$\Delta S_{b,i} = \sum_{j=1}^k \Delta\varepsilon_{p,b,i_j} \cdot h_j \quad (36)$$

459 where $\Delta\varepsilon_{p,b,i}$ is ballast permanent strain increment; i is iterative step; $\sigma_{d,b,i}$ is ballast
 460 dynamic deviatoric stress relevant to traffic load (in MPa); N_{lb} is the number of load cycles
 461 after the last ballast renewal/tamping; $\Delta S_{b,i}$ is ballast settlement increment; h_j is the
 462 thickness of each layer; k is number of sublayers. dN is the frequency of load application,
 463 for example where $dN = 1$ indicates every load passage is simulated, and $dN = 1000$
 464 indicates every 1000th load passage is simulated.



465

466

Figure 6. Comparison of proposed ballast settlement model with experimental data

467 4.3.2. Subgrade settlement

468 The subgrade settlement equation is a modified version of that proposed by Li and Selig (Li
 469 and Selig, 1996). Similar to the approach for calculating ballast settlement, it is modified to
 470 take into account the evolution of dynamic stress and to allow for the simulation of both
 471 newly constructed track and existing subgrade. The proposed, modified permanent strain
 472 increment and settlement increment at each iterative step are:

$$\Delta\varepsilon_{p_s,i} = \frac{a}{100} \left(\frac{\sigma_{d_s,i}}{\sigma_s} \right)^m \left[((dN \cdot i) + N_{ls})^b - ((dN \cdot (i - 1)) + N_{ls})^b \right] \quad (37)$$

$$\Delta S_{s,i} = \sum_{j=1}^k \Delta\varepsilon_{p_s,i_j} \cdot h_j \quad (38)$$

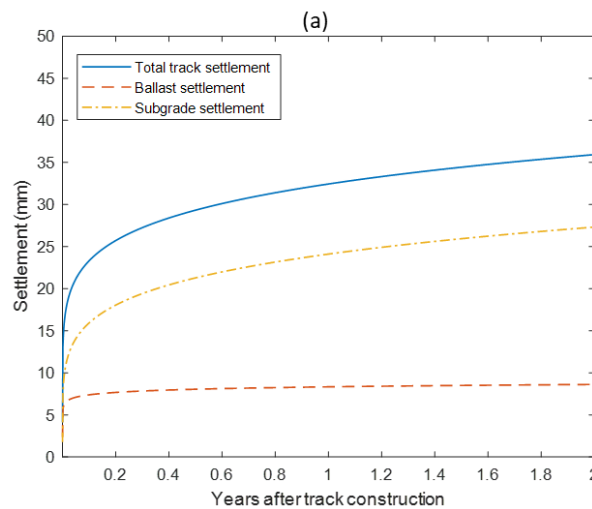
473 where $\Delta\varepsilon_{p_s,i}$ is subgrade permanent strain increment; $\sigma_{d_s,i}$ is subgrade dynamic deviatoric
 474 stress relevant to traffic load (in Pa); σ_s is soil compressive strength (in Pa); N_{ls} is the
 475 number of load cycles after the last subgrade replacement; $\Delta S_{s,i}$ is subgrade settlement
 476 increment; and a , m , and b are material parameters given in Table 1.

477 *Table 1 Settlement parameters a, b, and m for various subgrade soil types (Li and Selig, 1996)*

Material parameter	High-plasticity clay (CH)	Low-plasticity clay (CL)	High-plasticity silt (MH)	Low-plasticity silt (ML)
a	1.20	1.10	0.84	0.64
b	0.18	0.16	0.13	0.10
m	2.40	2.00	2.00	1.70

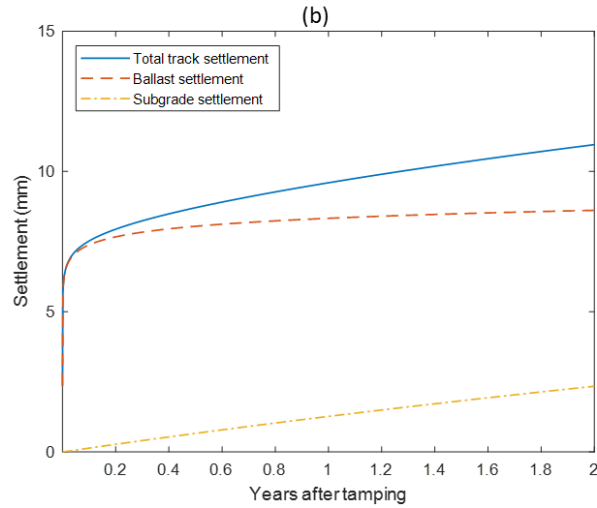
478

479 Figure 7 illustrates example settlement rates for three different cases. Figure 7(a) is the
 480 case of new track construction (newly placed ballast and soft subgrade) where a soft
 481 subgrade provides higher settlement than the ballast in the years after construction.
 482 Alternatively, Figure 7(b) is where the track has been compacted under several years of
 483 traffic loading, but the ballast has recently been renewed. In this case the ballast settlement
 484 exceeds the subgrade, particularly in the initial period after tamping. The third case, as seen
 485 in Figure 7(c), shows when the ballast and subgrade have both been in place for many years.
 486 The deformation rates of both ballast and subgrade increase slowly with increased load
 487 passages.

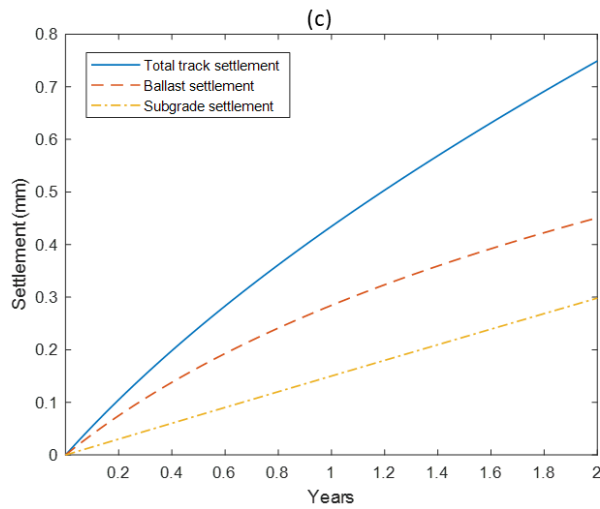


488

489



490



491 *Figure 7. Ballast, subgrade, and total track settlement: (a) a newly constructed track (b) an existing track following tamping*
 492 *and (c) an existing track that has not recently been tamped*

493 **4.3.3. Geostatic stress**

494 In addition to the stresses induced by quasi-static and dynamic loads, the stress field due to
 495 geostatic loading is also included in the settlement calculation. The vertical stress at a given
 496 location is calculated from the mass of the overlying material:

$$\sigma_V = \rho g h_z \tag{39}$$

497 where σ_V is the vertical stress; ρ is the density of the overlying material; g is gravity; and h_z
 498 is the vertical distance from the monitored point to the free surface.

499 Considering an unsaturated soil, the total stress is equal to the effective stress due to the
 500 absence of pore water pressure. The effective horizontal stress is approximated as a
 501 proportion of the effective vertical stress:

$$\sigma'_H = K'_0 \sigma'_V \tag{40}$$

$$\frac{\sigma'_H}{\sigma'_V} = K'_0 = \frac{\nu}{1-\nu} \tag{41}$$

502 where K'_0 is the coefficient of lateral stress (varying between 0 and 1.0).

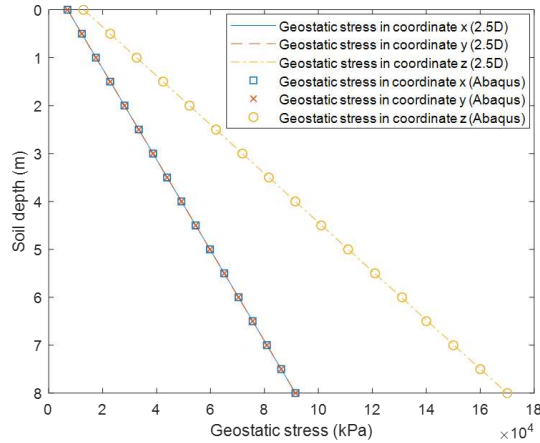


Figure 8. Geostatic stresses at the track centre

503

504

505 To check the accuracy of the geostatic stress calculation in the 2.5D model, geostatic
 506 stresses were calculated in the track, at the location of settlement computation. The results
 507 are compared with results from a 3D model, simulated using commercial FE software
 508 ABAQUS (Figure 8). The result is a strong fit.

509 Considering the stress field in 3D, the deviatoric stress is dependent on the sum of squares
 510 of the differences of the principal stresses:

$$\sigma_d = \sqrt{\frac{1}{2} \times \left[(\sigma_1 - \sigma_2)^2 + (\sigma_2 - \sigma_3)^2 + (\sigma_3 - \sigma_1)^2 \right]} \quad (42)$$

511 where σ_1 , σ_2 and σ_3 are the components of the principal stresses. Note that the total
 512 deviatoric stress includes the geo-static, quasi-static and dynamic stress components. It is
 513 calculated every 0.2m along track length (in the train passage direction) and at vertical
 514 depth intervals of 0.25m.

515

516 4.4. Detailed solution procedure

517 The previous sections outlined the general modelling strategy and key considerations. This
 518 section describes how they fit together to form the overall modelling methodology. Firstly,
 519 considering the two-step modelling approach (Figure 1), the sub-steps for the
 520 implementation of Step A are:

- 521 1. Calculate the geostatic stresses over the cross-section of the track structure
- 522 2. Determine the strain-adjusted material properties, considering non-linear material
 523 stiffness, due to quasi-static loading, using the 2.5D FEM-PML method
- 524 3. Compute the moving quasi-static and dynamic load transfer functions
- 525 4. Calculate the 3D stresses based on a unit load in the wavenumber-frequency domain
- 526 5. Compute the matrices of track compliance and train compliance

527 Step A only requires computation once, and when complete, the sub-steps for Step B are:

- 528 1. Calculate the train-track dynamic interaction forces based on the track irregularity
 529 profile and multi-body vehicle

- 530 2. Calculate the dynamic stresses along the entire track length. The calculation is
531 performed in the wavenumber-frequency domain and then transformed to obtain
532 the 3D dynamic stress fields in the time-space domain
- 533 3. Use the quasi-static, geostatic, and dynamic stresses to compute the deviatoric
534 stress (σ_d) using Eq. (42)
- 535 4. Compute the permanent strain increments and the settlement increments in ballast
536 and subgrade layers according to Eqs. (35) and (37) respectively
- 537 5. Obtain the differential track settlement over the entire track length
- 538 6. Update the track geometry irregularity and perform a domain transformation to
539 convert the updated signal into the spatial frequency domain
- 540 7. Return to step 1 and repeat the subsequent steps using the updated track geometry
541 irregularity
- 542 8. Stop when threshold reached (e.g. total cycles or standard deviation threshold)

543

544 5. Model validation

545 The following describes three validations confirming model accuracy. Firstly the dynamic
546 track-ground calculation is validated, followed by the train-track interaction forces, and
547 finally differential settlement.

548 5.1. Validation case 1: Track-ground dynamics and non-linearity

549 Case 1 is used to validate the model's ability to simulate track-ground dynamics and non-
550 linear behaviour using an iterative linear equivalent procedure. The validation is performed
551 using data from the case of a soft soil site at Ledsgard, Sweden (Madshus and Kaynia, 2000).
552 This site experienced large deflections under the passage of X2000 trains shortly after
553 opening, attributed to critical velocity effects (Connolly et al., 2020; Connolly and Costa,
554 2020), leading to soil non-linearity.

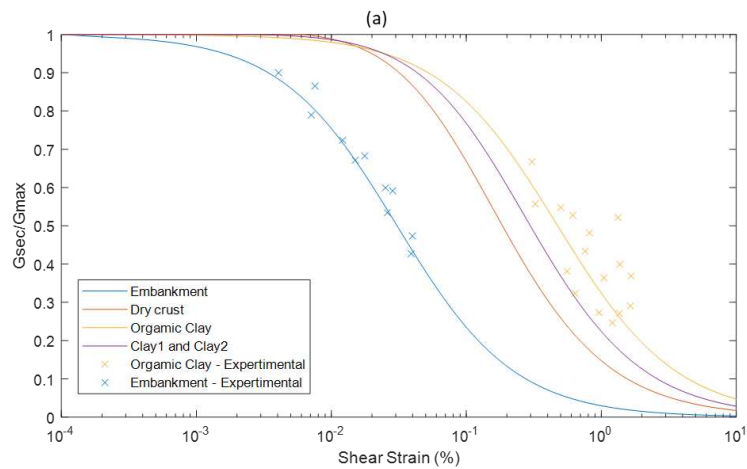
555 Regarding the material properties at the site, the UIC60 rail is continuously supported by
556 railpads with a stiffness of 255×10^6 N/m² and a damping coefficient of 22.5×10^3 Ns/m². The
557 sleepers are simulated using the aforementioned anisotropic constitutive model, with a
558 Young's modulus of 30GPa. The low-strain soil properties are based on field test results and
559 shown in Table 2. The experimental data for organic clay is taken from (Alves Costa et al.,
560 2010). Embankment material properties are based on experimental data from (Dyvik and
561 Kaynia, 2018). Figure 9(a) and (b) show the shear modulus reduction and damping ratio
562 curves obtained using the empirical equations proposed by (Rollins et al., 2020b) for the
563 embankment, and (Ishibashi and Zhang, 1993) for the other soil layers. Train loading
564 information is available in (Dong et al., 2019).

565

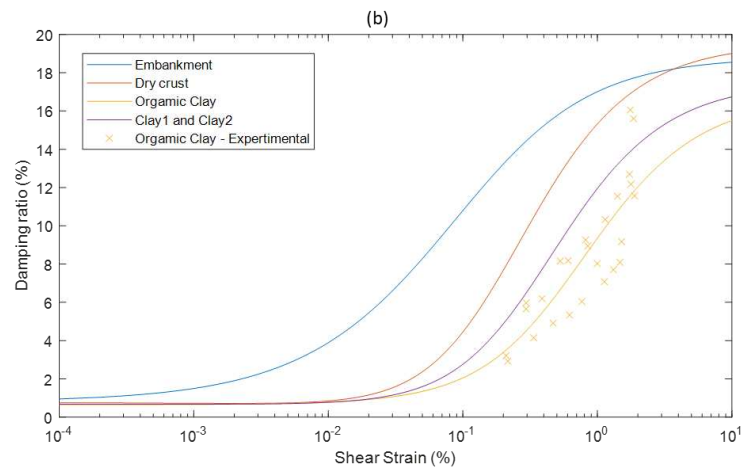
Table 2. Small-strain properties at Ledsgard

Layer	Thickness (m)	Density (kg/m ³)	P-wave speed (m/s)	S-wave speed (m/s)	Damping ratio
Embankment	1.2	1800	210	340	0.04
Dry crust	1.1	1500	63	500	0.04
Organic clay	3.5	1260	41	500	0.02
Clay 1	4.5	1475	60	1500	0.05
Clay 2	6.0	1475	87	1500	0.05

566



567



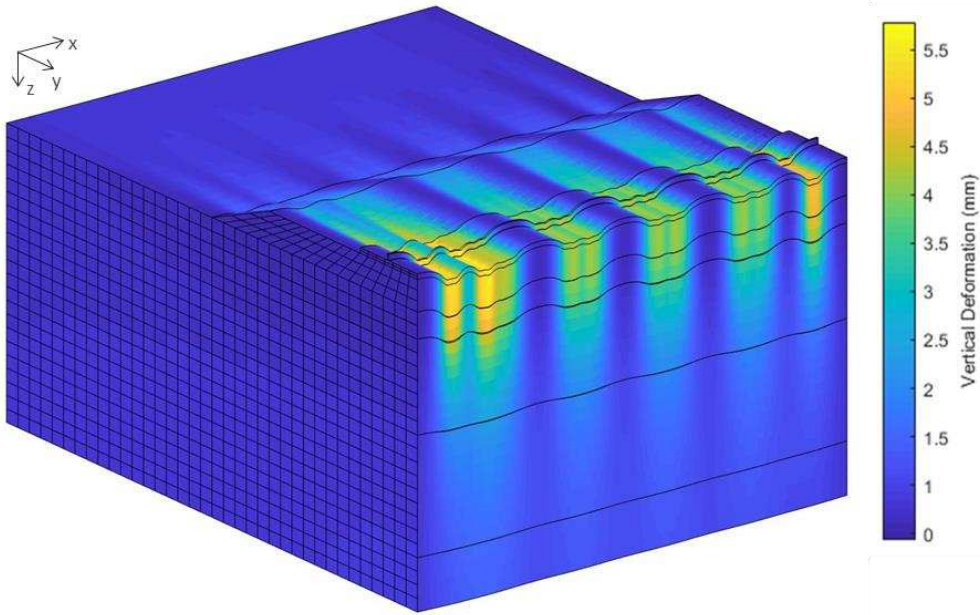
568

569

Figure 9. Non-linear soil characteristics (a) shear modulus reduction curves (b) damping ratio

570 The 3D track-ground displacement contour for a 70km/h train is illustrated in Figure 10. The
 571 deflection contours are visible and show the response propagating from the rail into
 572 supporting track-ground structure. Figure 11(a) and (b) show the examples of time histories
 573 of displacements calculated with and without considering non-linear effects, and compared
 574 with the field data for speeds of 70 km/h and 140 km/h, respectively. It can be seen that
 575 the results predicted by the non-linear simulation are a significantly better fit than the linear
 576 simulation. This is consistent with the works of (Dong et al., 2019) and (Alves Costa et al.,
 577 2010), and confirms the model's ability to simulate the non-linear part of the response.
 578 Figure 11(c) compares the peak upward and downward displacements between the field
 579 data, the linear simulation and the non-linear simulation for speeds ranging from 70 to 205
 580 km/h. The comparison reveals that the results from a non-linear formulation are again a
 581 closer match with the field data. Therefore, it can be concluded that the model is capable of
 582 accurately calculating railway track deflections, regardless of whether the strain levels
 583 induce non-linear behaviour or not.

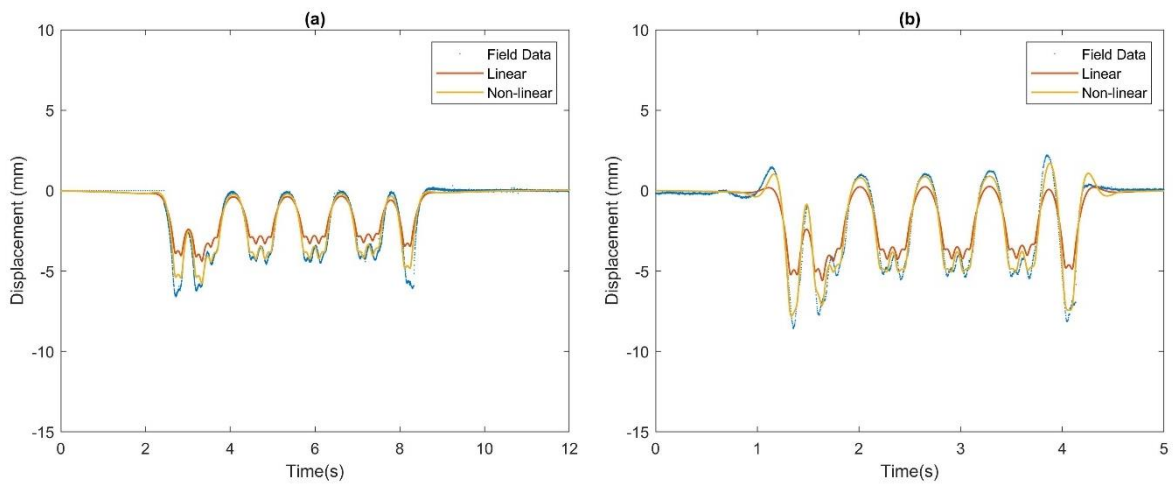
584



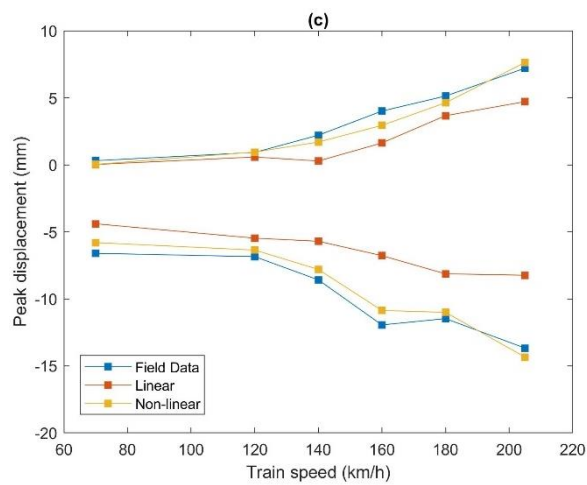
585

586

Figure 10. 3D track-ground deflection profile (slice along track centreline)



587



588

589

590

Figure 11. Measured and simulated time histories of track displacements for different train speeds (Southbound): (a) speed = 70km/h (b) speed = 140km/h (c) peak displacements versus train speeds

591 **5.2. Validation case 2: Train-track interaction**

592 Case 2 is used to validate the frequency-wavenumber domain solution method for train-
 593 track interaction. This is important for accurately calculating the forces that lead to the
 594 stresses in the track-subgrade. The validation is performed using an artificial track
 595 irregularity profile defined by FRA (Federal Railroad Administration, 1980) Class 5 for
 596 wavelengths in the range $3 < \lambda \leq 25 \text{ m}$. The model of train-track dynamic interaction in the
 597 frequency domain is validated against an equivalent time domain FE model (Thompson,
 598 2008) solved using an implicit integration scheme. The time domain model is governed by:

$$F_{dyn} = \frac{i\omega r Y_r}{Y_r + Y_w + Y_c} \quad (43)$$

$$Y_r = \frac{i\omega u_{max}}{F_{sta}} \quad (44)$$

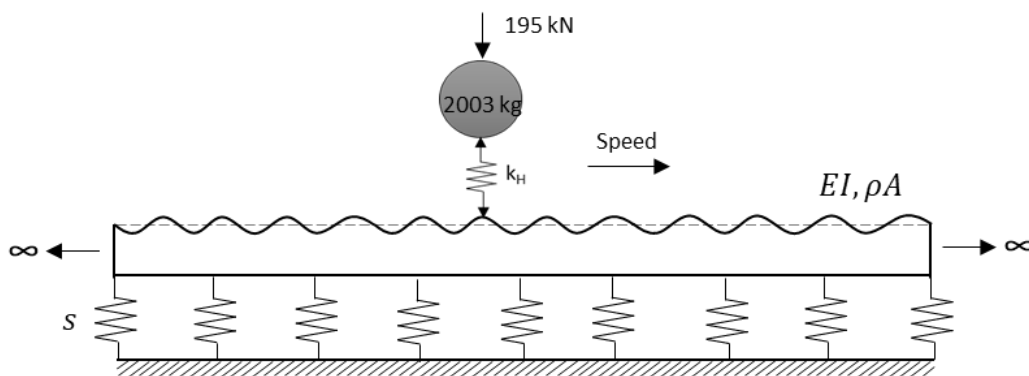
$$Y_w = \frac{-i}{\omega M_w} \quad (45)$$

$$Y_c = \frac{i\omega}{k_H} \quad (46)$$

599 where $i\omega r$ is the roughness velocity amplitude; Y_r is the vertical rail mobility; Y_w is the
 600 wheel mobility; Y_c is the contact spring mobility; u_{max} is the maximum displacement due to
 601 static load; F_{sta} is the static load; and M_w is the wheelset mass.

602 The validation is a simplified 2D model of a railway track as shown in Figure 12. The rail is
 603 represented using an infinite Euler-Bernoulli beam supported by a single continuous elastic
 604 layer. It has the following material properties: Young's modulus $E = 2.1 \times 10^{11} \text{ N/m}^2$; second
 605 moment of area $I = 30.55 \times 10^{-6} \text{ m}^4$; cross section area $A = 0.00763 \text{ m}^2$; density $\rho =$
 606 7850 kg/m^3 ; and support stiffness $s = 1 \times 10^8 \text{ N/m}^2$. A single axle vehicle travels across the
 607 structure at speed of 150 km/h, with wheel mass $M_w = 2003 \text{ kg}$. The load on the wheel
 608 (from weight of the vehicle) is 195 kN.

609



610

611 *Figure 12. Simplified 2D train-track interaction problem*

612 Figure 13 shows a comparison of displacement time histories between the time domain
 613 model and the frequency domain model. It should be noted that the displacements are only
 614 due to the dynamic load and not combined with the quasi-static load. A good match of the
 615 results confirms the accuracy of the train-track dynamic interaction model.

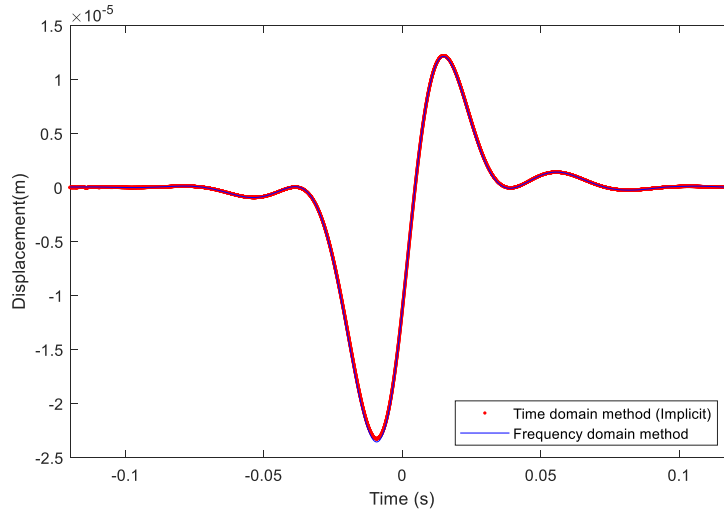


Figure 13. A comparison of displacement time histories due to dynamic loading

616

617

618

619 5.3. Validation case 3: Differential settlement

620 Case 3 is used to validate the model's ability to compute the evolution of vertical track
 621 geometry with increasing axle passages. Historical track geometry data, from a track section
 622 in the UK, is used for comparison. The data was collected using a track recording vehicle,
 623 and the standard deviation of the vertical track irregularity profile over a 200m track length
 624 is considered. Considering an aim of the model is to predict tamping intervals, only
 625 wavelengths in the 3-25m range are considered.

626 The site investigation data was collated and the properties of the track and subgrade are
 627 shown in Table 3. The subgrade is ML soil type (silt) with a shear strength of 25 kPa. The soil
 628 strength parameters a , b and m for the subgrade settlement equation are 0.64, 0.10, and
 629 1.7 respectively. The site was specifically selected to have minimal freight traffic, thus
 630 reducing the variation in rolling-stock types. The dominant train properties are based upon
 631 the British Rail Class 390 Pendolino as shown in Table 4. Regarding the traffic condition, the
 632 line speed is 201 km/h with annual tonnage of 37 million gross tonnes (MGT), 98% of which
 633 is passenger. Over a year period, track geometry was measured on 04-01-2017, 26-04-2017,
 634 16-08-2017, and 16-12-2017, and no tamping took place between these dates.

635

Table 3. Ballasted track properties

Component	Parameter	Value
UIC 60 Rail (single rail)	Height (m)	0.172
	Length in transversal direction (m)	0.015
	Section area (m ²)	7.677x10 ³
	Moment of Inertia y-y (m ⁴)	3.038x10 ⁻⁵
	Moment of Inertia z-z (m ⁴)	0.512x10 ⁻⁵
	Young's modulus (Pa)	2.11x10 ¹¹
	Density (kg/m ³)	7850
	Poisson's ratio	0.3
	Hysteric damping coefficient	0.01
Railpad (spring element)	Continuous stiffness (N/m)	255x10 ⁶
	Viscous damping (Ns ² /m)	22.5x10 ³

Component	Parameter	Value
Sleeper (G44)	Height (m)	0.2
	Length in transversal direction (m)	2.5
	Sleeper spacing (m)	0.65
	Young's modulus (Pa)	3×10^{10}
	Density (kg/m^3)	2500
	Poisson's ratio	0.2
	Hysteric damping coefficient	0.01
Ballast	Height (m)	0.3
	Length in transversal direction (m)	2.8
	Young's modulus (Pa)	97×10^6
	Density (kg/m^3)	1591
	Poisson's ratio	0.12
	Hysteric damping coefficient	0.061
Sub-ballast	Height (m)	0.5
	Length in transversal direction (m)	3.5
	Young's modulus (Pa)	212×10^6
	Density (kg/m^3)	1913
	Poisson's ratio	0.3
	Hysteric damping coefficient	0.054
Subgrade	Young's modulus (Pa)	60×10^6
	Density (kg/m^3)	2000
	Poisson's ratio	0.35
	Hysteric damping coefficient	0.03

636

637

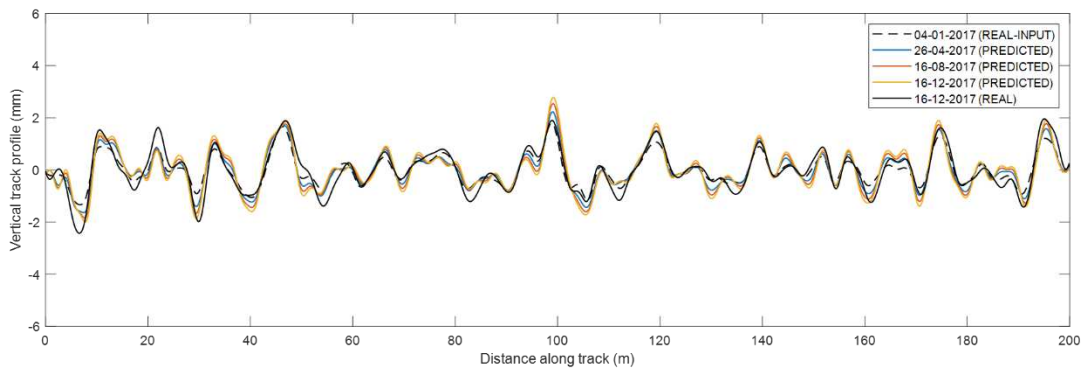
Table 4. Pendolino (Class 390) parameters

Parameter	Value
Axle spacing (m)	2.7
Bogie spacing (m)	17
Car body mass (kg)	475×10^2
Car body pitching moment of inertia (kg.m^2)	206×10^4
Bogie mass (kg)	2325
Wheelset mass (kg)	1750
Bogie pitching moment of inertia (kg.m^2)	3000
Primary suspension stiffness (Nm^{-1})	258×10^3
Primary suspension viscous damping (Nsm^{-1})	4250
Secondary suspension stiffness (Nm^{-1})	410×10^3
Secondary suspension viscous damping (Nsm^{-1})	200×10^2

638

639 The initial vertical track profile, measured on 04-01-2017 was used as the starting geometry.
640 The model then simulated and updated the track geometry profile, after every individual
641 load passage, based upon expected MGT. Over the course of almost a year, the evolving
642 track geometry profiles are shown in Figure 14. The predicted profile for the final track
643 recording is also shown and compared against the numerical simulation. It is seen that the
644 amplitudes are closely matched in phase and amplitude. There are some discrepancies,
645 however these are most likely due to varying track-ground material properties along the

646 track section, which are difficult to capture from a single-point site investigation, and the
647 fact that the true traffic was not 100% Pendolino rolling stock.

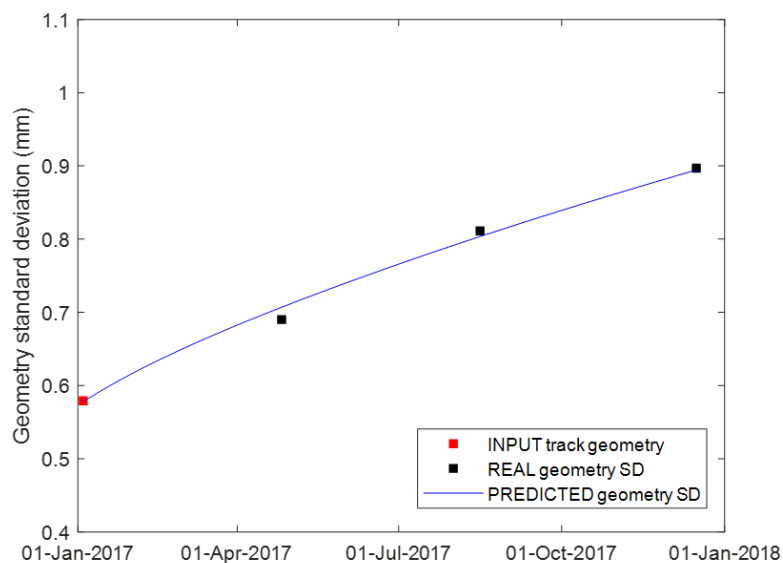


648

649

Figure 14. Vertical track profile. Predicted profile vs field data

650 Figure 15 compares the recorded and predicted evolution of geometry SD at the site. The
651 rectangular markers are the real geometry SD from the recording car, and the red marker is
652 the SD of the initial vertical track profile. The blue solid line is the predicted geometry SD
653 updated after every load cycle during simulation. Compared to the real data, it is seen that
654 the predicted geometry SD curve is a strong match to the recording data. This result,
655 combined with the results in Figure 14, shows the strong ability of the model to accurately
656 predict differential settlement and standard deviation evolution.



657

658

Figure 15. Evolution of standard deviation with time. Predicted values vs field data

659

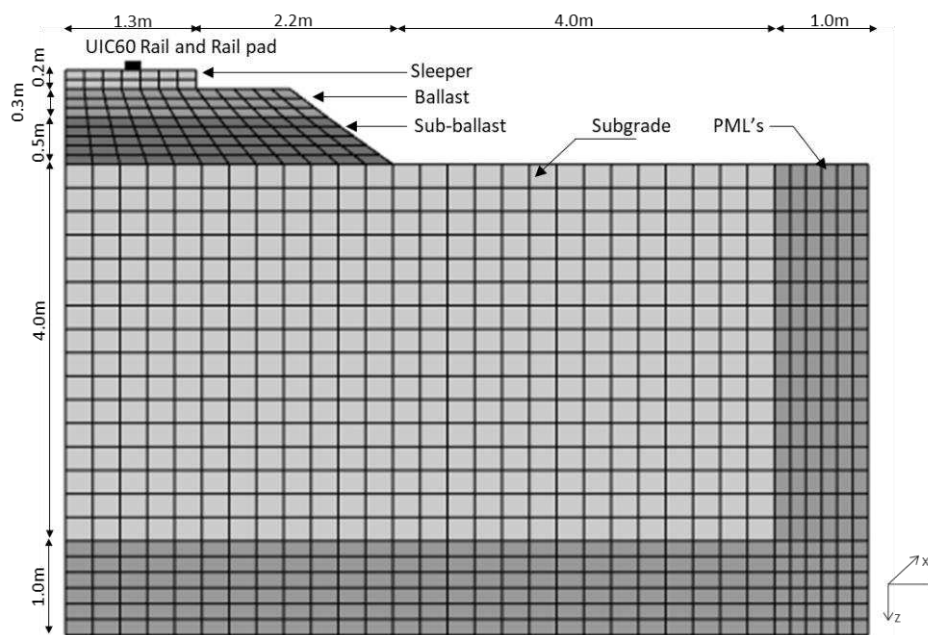
660 6. Analysis

661 The validated model is used to perform 2 analyses. First it is used to analyse the effect of
662 the frequency of updating track geometry on differential settlement. Three cases are
663 simulated: updating it after every axle passage, updating after every 10 passages, and also
664 after every 100 passages. Secondly, the model is used to investigate the role of settlement

665 parameters in the subgrade settlement model. Four cases are simulated: a low-plasticity silt
 666 (ML), a high-plasticity silt (MH), a low-plasticity clay (CL), and a high-plasticity clay (CH).
 667 Prior to the analyses the model input properties are defined.

668
 669 **6.1. Model properties**

670 Figure 16 shows the finite element mesh used for the numerical analysis. The
 671 characteristics of the rails, rail pads, sleepers, ballast and sub-ballast are the same as
 672 described in Table 3. Two different subgrades are considered, with their geotechnical
 673 properties shown in Table 5. They are chosen to represent a stiff and soft soil respectively,
 674 with Young's modulus being their only differentiating parameter. The vehicle is a Pendolino
 675 train travelling at 201 km/h, with properties shown in Table 4.



676
 677 *Figure 16. Finite element mesh*

678 *Table 5 Subgrade properties*

Parameter	Soil case 1	Soil case 2
Young's modulus (Pa)	120x10 ⁶	60x10 ⁶
Density (kg/m ³)	2000	2000
Poisson's ratio	0.3	0.3
Hysteric damping coefficient	0.03	0.03
Primary wave speed (m/s)	284	201
Secondary wave speed (m/s)	152	107

679
 680 **6.2. Track irregularity**

681 A synthetic irregularity profile is used, where the irregularities are generated using a PSD
 682 function, where the spatial frequency is $k_x = \frac{2\pi}{\lambda_{irr}}$, and λ_{irr} represents the wavelength of the
 683 irregularity. The formulation is based on FRA (Federal Railroad Administration, 1980) and
 684 has the following form:

$$S_n(k_x) = \frac{Ak_3^2(k_x^2 + k_2^2)}{k_x^4(k_x^2 + k_3^2)} \quad (47)$$

685 where A is a roughness constant, while k_2 and k_3 spatial frequency constants.

686 After computing the PSD, the amplitude of unevenness in terms of the spatial frequency is:

$$\delta u_j = \left(\sqrt{2S_n(k_{x_j})} \Delta k_x \right) e^{-i\theta_j} \quad (48)$$

687 where Δk_x is the resolution retained for the spatial frequency, and θ is phase angle, taken
688 as a random variable with uniform distribution in the range 0 to 2π .

689 Since the track quality is defined using SD over distance along track, the initial track profile
690 in terms of position x is obtained using:

$$u_{irr}(x) = \sum_{j=1}^N \delta u_j e^{ik_{x_j}x} \quad (49)$$

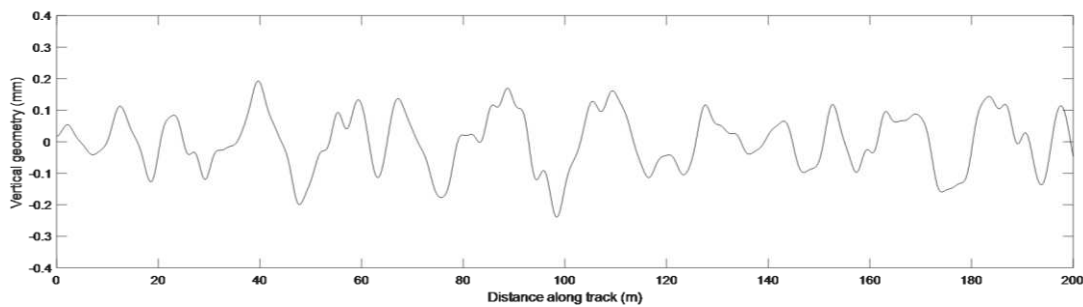
691

692 6.3. Influence of updating the track geometry after each axle load

693 To understand how frequently the track geometry profile requires updating between load
694 passage simulations, the two subgrade cases are subject to 100,000 axle loads. The
695 simulations are performed with three different values of: $dN=1, 10$ and 100 . This means the
696 track irregularity profile, train-track dynamic interaction forces, and deviatoric stresses are
697 updated every 1, 10, and 100 load passages until the total number of passages is reached.
698 In practical terms, considering an initial track geometry, $dN=100$ means that all profile
699 changes due to the next 100 axle loads are not explicitly modelled. Instead, after 100 cycles,
700 the model attempts to update the profile considering the cumulative change due to the
701 previous 100 cycles.

702 The number of loading applications after the last renewal of ballast and subgrade,
703 N_{lb} and N_{ls} , are equal to zero, representing the case of newly constructed track that has
704 only experienced minimal traffic loading. Both subgrade soils are silty sand, with material
705 parameters (a, m, b) given in Table 1.

706 The initial track irregularity profile is artificially generated using the PSD function defined by
707 FRA, considering 40 frequencies, and is shown in Figure 17. In order to represent a new
708 track, constructed to tight tolerances and prior to significant train loading, the value of
709 parameter A is set as $0.29 \times 10^{-8} \text{ m}^2\text{-rad/m}$.



710

711

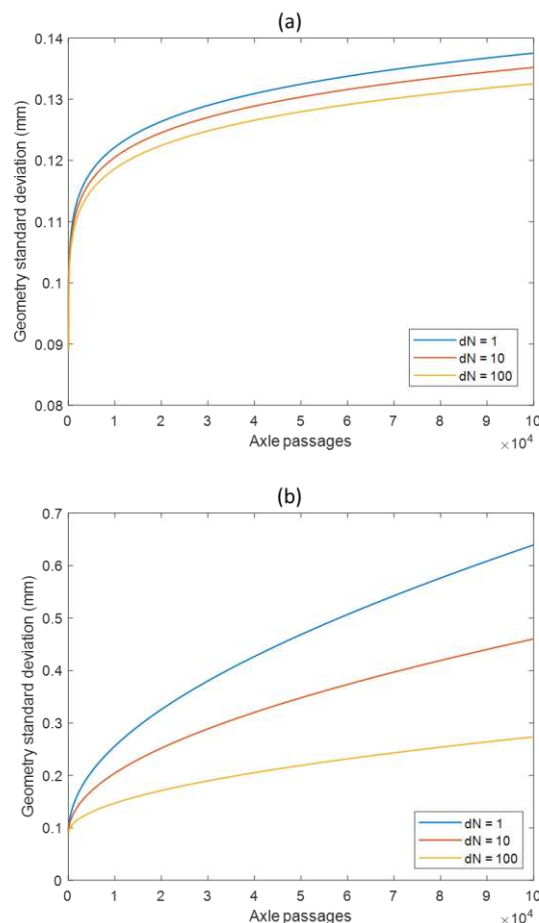
Figure 17. Initial track irregularity profile

712

713 Considering Soil case 1 (high stiffness soil), Figure 18(a) shows the change in geometry
714 standard deviation versus load cycles, for dN=1, dN=10, and dN=100. After 100k cycles, it is
715 seen that dN = 1 results in the highest standard deviation, while dN=100 results in the track
716 geometry with lowest standard deviation. The discrepancy between using dN=10 rather
717 than dN=1 is 2.17%, while the discrepancy between using dN=100 rather than dN=1 is
718 3.62%.

719 Similar findings are true for Soil case 2 (lower stiffness soil), however the effect is more
720 pronounced, as shown in Figure 18(b). dN=1 results in the highest standard deviation, while
721 dN=100 results in the lowest. The discrepancy between using dN=10 rather than dN=1 is
722 32.07%, while the discrepancy between using dN=100 rather than dN=1 is 65.43%.

723 These findings indicate that it is important to update the track geometry profile as
724 frequently as possible, and ideally after every load passage. Although this implies increased
725 computational effort, if not adhered to, then the full effect of train-track interaction on
726 differential settlement is not captured. This is particularly true for softer soils where the
727 effect is amplified.



728

729

730 *Figure 18. Track geometry evolution versus profile update frequency: (a) high stiffness subgrade; (b) low stiffness subgrade*

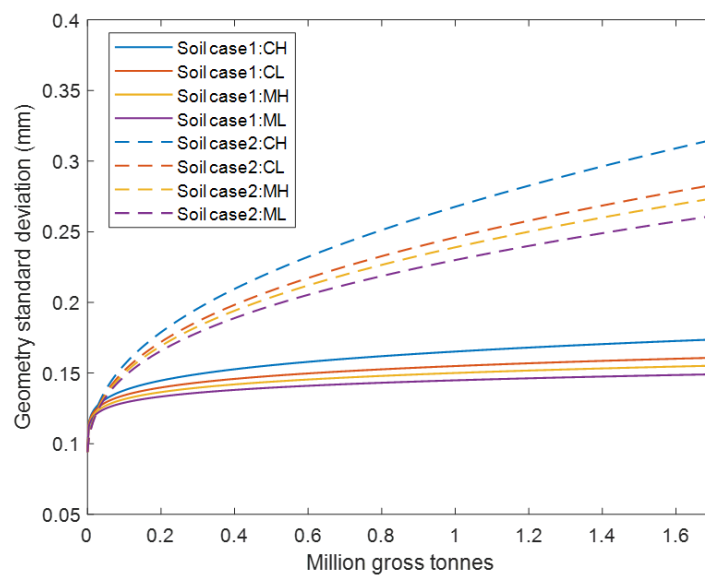
731

732 **6.4. Influence of subgrade material properties**

733 The subgrade material model is characterised by: 1) elastodynamic properties, that describe
734 the propagation of stress fields, and 2) settlement properties that describe how these stress

735 fields result in settlement. To understand the relation between these properties, a
736 sensitivity analysis is performed by changing the Young's modulus and also the settlement
737 parameters (a, b and m). The two Young's modulus properties are shown in Table 5, while
738 the four settlement combinations are shown in Table 1. It should be noted that the
739 sensitivity analysis was performed to understand the relationship between parameters,
740 rather than to attempt to simulate any specific soil types.

741 Figure 19 shows the change in geometry standard deviation versus load cycles, for changing
742 settlement parameters: ML, MH, CL, CH, and for the stiff and soft soils. Considering Soil
743 case 1 (stiff), the standard deviation for a ML soil is 0.149mm. For the other soil types, the
744 standard deviation increases by 4.09%, 7.84% and 16.49% for MH, CL and CH respectively.
745 Similar is true for Soil case 2 (soft), where the same soil types cause increases of 4.74%,
746 8.38% and 20.66% respectively. Therefore it can be concluded that the higher the clay
747 content in the soil, the larger the settlement. However, although the settlement
748 parameters have a marked difference on track geometry, the difference between the soft
749 and stiff soil is even greater. The soft soil has a significantly higher standard deviation for all
750 settlement parameters, which shows the importance of subgrade stiffness on track
751 performance.



752

753

Figure 19. Track geometry evolution for varying subgrade properties

754 It is seen that both elastodynamic and settlement properties significantly influence on the
755 evaluation of track geometry profile and deterioration. These properties are directly
756 relevant to different soil types. However, there are still a number of influential variables
757 that affect the track and the vehicle. Therefore, design charts can possibly be developed
758 after performing more analyses.

759

760 7. Conclusions

761 Track geometry is an important parameter for scheduling track maintenance operations.
762 Therefore this paper presents a novel numerical approach, capable of predicting track

763 irregularity evolution for a wide range of situations. It has the following novel
764 characteristics:

- 765 1. It's solved using a mixed frequency-wavenumber and time-space approach. This
766 optimised solution procedure then allows for the track geometry profile to be
767 updated after every load passage
- 768 2. The track and ground are fully coupled and modelled explicitly. This allows for 3D
769 stress fields to be computed, which are important for accurate settlement
770 calculation
- 771 3. The effect of strain on track and ground material properties is accounted for using an
772 iterative equivalent linear approach
- 773 4. Modified settlement laws are used that can account for the differing forces induced
774 due to evolving track profiles

775 Three aspects of the model are validated. These are its ability to accurately simulate track
776 deflections and non-linearity, its ability to model train-track interaction, and its ability to
777 predict future changes in vertical track profile. The validated model is then used to
778 investigate the influence of updating the track geometry after each axle load on the
779 differential settlement prediction. This confirms the importance of updating the track
780 geometry profile as frequently as possible, particularly for softer soils. In addition, the
781 effect of changing the elastodynamic and settlement properties of the subgrade are
782 investigated. It is shown that stiffer soils give rise to markedly reduced settlement, thus
783 highlighting the need for well-constructed track subgrade.

784

785 **8. Acknowledgements**

786 The authors are grateful to Network Rail for providing track geometry data, the University of
787 Leeds, the Cheney fellowship scheme and the Leverhulme Trust UK (PLP-2016-270). They
788 also acknowledge the financial support provided by the Spanish Ministries Science and
789 Innovation and Universities under research project PID2019-109622RB-C21, and US-126491
790 funded by the FEDER Andalucía 2014-2020 Operational Program. Shift2Rail and IN2TRACK3
791 are also acknowledged.

792 **Author contributions**

793 C. Charoenwong: methodology, software, analysis, writing; D. P. Connolly:
794 conceptualisation, methodology, resources, writing, supervision; P. Woodward: Reviewing;
795 P. Galvin: supervision, writing; P. Alves Costa: supervision, writing

796 **References**

797 Abadi T, Le Pen L, Zervos A, Powrie W. A Review and Evaluation of Ballast Settlement
798 Models using Results from the Southampton Railway Testing Facility (SRTF). *Procedia Eng*
799 2016;143:999–1006. <https://doi.org/10.1016/j.proeng.2016.06.089>.

800 Alves Costa P, Calçada R, Silva Cardoso A, Bodare A. Influence of soil non-linearity on the
801 dynamic response of high-speed railway tracks. *Soil Dyn Earthq Eng* 2010;30:221–35.
802 <https://doi.org/10.1016/j.soildyn.2009.11.002>.

803 Arcos R, Soares PJ, Alves Costa P, Godinho L. An experimental/numerical hybrid

804 methodology for the prediction of railway-induced ground-borne vibration on buildings to
805 be constructed close to existing railway infrastructures: Numerical validation and parametric
806 study. *Soil Dyn Earthq Eng* 2021;150:106888.
807 <https://doi.org/10.1016/j.soildyn.2021.106888>.

808 Bian X, Jiang H, Chang C, Hu J, Chen Y. Track and ground vibrations generated by high-speed
809 train running on ballastless railway with excitation of vertical track irregularities. *Soil Dyn*
810 *Earthq Eng* 2015;76:29–43. <https://doi.org/10.1016/j.soildyn.2015.02.009>.

811 Burrow MPN, Shi J, Wehbi M, Ghataora GS. Assessing the damaging effects of railway
812 dynamic wheel loads on railway foundations. *Transp Res Rec* 2017;2607:62–73.
813 <https://doi.org/10.3141/2607-09>.

814 Chen C, McDowell GR. An investigation of the dynamic behaviour of track transition zones
815 using discrete element modelling. *Proc Inst Mech Eng Part F J Rail Rapid Transit*
816 2016;230:117–28. <https://doi.org/10.1177/0954409714528892>.

817 Colaço A, Costa PA, Connolly DP. The influence of train properties on railway ground
818 vibrations. *Struct Infrastruct Eng* 2016;12:517–34.
819 <https://doi.org/10.1080/15732479.2015.1025291>.

820 Connolly DP, Costa PA. Geodynamics of very high speed transport systems. *Soil Dyn Earthq*
821 *Eng* 2020;130:105982. <https://doi.org/10.1016/j.soildyn.2019.105982>.

822 Connolly DP, Dong K, Alves Costa P, Soares P, Woodward PK. High speed railway ground
823 dynamics: a multi-model analysis. *Int J Rail Transp* 2020;8:324–46.
824 <https://doi.org/10.1080/23248378.2020.1712267>.

825 Cooley JW, Tukey JW. An Algorithm for the Machine Calculation of Complex Fourier Series
826 Published by : American Mathematical Society Stable URL :
827 <https://www.jstor.org/stable/2003354> REFERENCES Linked references are available on
828 JSTOR for this article : An Algorithm for the M 2019;19:297–301.

829 Costa PA, Calçada R, Cardoso AS. Influence of train dynamic modelling strategy on the
830 prediction of track-ground vibrations induced by railway traffic. *Proc Inst Mech Eng Part F J*
831 *Rail Rapid Transit* 2012;226:434–50. <https://doi.org/10.1177/0954409711433686>.

832 Dahlberg T. Some railroad settlement models - A critical review. *Proc Inst Mech Eng Part F J*
833 *Rail Rapid Transit* 2001;215:289–300. <https://doi.org/10.1243/0954409011531585>.

834 Dong K, Connolly DP, Laghrouche O, Woodward PK, Alves Costa P. Non-linear soil behaviour
835 on high speed rail lines. *Comput Geotech* 2019;112:302–18.
836 <https://doi.org/10.1016/j.compgeo.2019.03.028>.

837 Dyvik R, Kaynia AM. Large-Scale Triaxial Tests on Railway Embankment Material. In: Stark T,
838 Swan R, Szecsy R, editors. *Railr. Ballast Test. Prop.*, West Conshohocken, PA: ASTM
839 International; 2018, p. 173–90. <https://doi.org/10.1520/STP160520170031>.

840 Esveld C. *Modern railway track*. vol. 385. MRT-productions Zaltbommel; 2001.

841 Federal Railroad Administration. *Statistical Representations of Track Geometry : Volume I*.
842 Washington, D.C.: 1980.

843 François S, Schevenels M, Galvín P, Lombaert G, Degrande G. A 2.5D coupled FE-BE
844 methodology for the dynamic interaction between longitudinally invariant structures and a
845 layered halfspace. *Comput Methods Appl Mech Eng* 2010.
846 <https://doi.org/10.1016/j.cma.2010.01.001>.

847 Fröhling RD. Prediction of Spatially Varying Track Settlement. *Conf Railw Eng CORE98*
848 1998:103–9.

849 Grossoni I, Powrie W, Zervos A, Bezin Y, Le Pen L. Modelling railway ballasted track
850 settlement in vehicle-track interaction analysis. *Transp Geotech* 2021;26:100433.
851 <https://doi.org/10.1016/j.trgeo.2020.100433>.

852 Guo Y, Zhai W. Long-term prediction of track geometry degradation in high-speed vehicle–
853 ballastless track system due to differential subgrade settlement. *Soil Dyn Earthq Eng*
854 2018;113:1–11. <https://doi.org/10.1016/j.soildyn.2018.05.024>.

855 Guo Y, Zhao C, Markine V, Jing G, Zhai W. Calibration for discrete element modelling of
856 railway ballast: A review. *Transp Geotech* 2020;23:100341.
857 <https://doi.org/10.1016/j.trgeo.2020.100341>.

858 Hardin BO, Drnevich VP. Shear modulus and damping in soils: design equations and curves. *J*
859 *Soil Mech Found Div* 1972;98:667–92.

860 Hardy GH, Littlewood JE. An additional note on Parseval’s theorem. *Math Zeitschrift* n.d.;34.

861 Indraratna B, Nimbalkar S. Stress-Strain Degradation Response of Railway Ballast Stabilized
862 with Geosynthetics. *J Geotech Geoenvironmental Eng* 2013;139:684–700.
863 [https://doi.org/10.1061/\(asce\)gt.1943-5606.0000758](https://doi.org/10.1061/(asce)gt.1943-5606.0000758).

864 Indraratna B, Thakur PK, Vinod JS. Experimental and numerical study of railway ballast
865 behavior under cyclic loading. *Int J Geomech* 2010;10:136–44.

866 Indraratna B, Thakur PK, Vinod JS, Salim W. Semiempirical Cyclic Densification Model for
867 Ballast Incorporating Particle Breakage. *Int J Geomech* 2012;12:260–71.
868 [https://doi.org/10.1061/\(asce\)gm.1943-5622.0000135](https://doi.org/10.1061/(asce)gm.1943-5622.0000135).

869 Ishibashi I, Zhang X. Unified dynamic shear moduli and damping ratio of sand and clay. *Soils*
870 *Found* 1993;33:182–91.

871 Karlström A, Boström A. An analytical model for train-induced ground vibrations from
872 railways. *J Sound Vib* 2006;292:221–41. <https://doi.org/10.1016/j.jsv.2005.07.041>.

873 Knothe K, Wu Y. Receptance behaviour of railway track and subgrade. *Arch Appl Mech*
874 1998;68:457–70. <https://doi.org/10.1007/s004190050179>.

875 Kouroussis G, Connolly DP, Verlinden O. Railway-induced ground vibrations – a review of
876 vehicle effects. *Int J Rail Transp* 2014;2:69–110.
877 <https://doi.org/10.1080/23248378.2014.897791>.

878 Lee JS, Hwang SH, Choi IY, Choi Y. Deterioration Prediction of Track Geometry Using Periodic
879 Measurement Data and Incremental Support Vector Regression Model. *J Transp Eng Part A*
880 *Syst* 2020;146:04019057. <https://doi.org/10.1061/jtepbs.0000291>.

881 Li D. Railway track granular layer thickness design based on subgrade performance under

882 repeated loading. University of Massachusetts, Amherst, Mass, 1994.

883 Li D, Hyslip J, Sussmann T, Chrismer S. Railway geotechnics. CRC Press; 2015.

884 Li D, Selig ET. Cumulative Plastic Deformation for Fine-Grained Subgrade Soils. *J Geotech Eng*
885 1996;122:1006–13. [https://doi.org/10.1061/\(asce\)0733-9410\(1996\)122:12\(1006\)](https://doi.org/10.1061/(asce)0733-9410(1996)122:12(1006)).

886 Li X, Ekh M, Nielsen JCO. Three-dimensional modelling of differential railway track
887 settlement using a cycle domain constitutive model. *Int J Numer Anal Methods Geomech*
888 2016;40:1758–70.

889 Liu J, Xiao J. Experimental Study on the Stability of Railroad Silt Subgrade with Increasing
890 Train Speed. *J Geotech Geoenvironmental Eng* 2010;136:833–41.
891 [https://doi.org/10.1061/\(asce\)gt.1943-5606.0000282](https://doi.org/10.1061/(asce)gt.1943-5606.0000282).

892 Lopes P, Costa PA, Ferraz M, Calçada R, Cardoso AS. Numerical modeling of vibrations
893 induced by railway traffic in tunnels: From the source to the nearby buildings. *Soil Dyn*
894 *Earthq Eng* 2014;61–62:269–85. <https://doi.org/10.1016/j.soildyn.2014.02.013>.

895 Madhus C, Kaynia AM. High-speed railway lines on soft ground: dynamic behaviour at
896 critical train speed. *J Sound Vib* 2000;231:689–701. <https://doi.org/10.1006/jsvi.1999.2647>.

897 Menan Hasnayn M, John McCarter W, Woodward PK, Connolly DP, Starrs G. Railway
898 subgrade performance during flooding and the post-flooding (recovery) period. *Transp*
899 *Geotech* 2017;11:57–68. <https://doi.org/10.1016/j.trgeo.2017.02.002>.

900 Network Rail. Track geometry - Inspections and minimum actions - NR/L2/TRK/001/mod11.
901 London, UK: 2015.

902 Neuhold J, Landgraf M, Marschnig S, Veit P. Measurement Data-Driven Life-Cycle
903 Management of Railway Track. *Transp Res Rec* 2020;2674:685–96.
904 <https://doi.org/10.1177/0361198120946007>.

905 Nielsen JCO, Li X. Railway track geometry degradation due to differential settlement of
906 ballast/subgrade – Numerical prediction by an iterative procedure. *J Sound Vib*
907 2018;412:441–56. <https://doi.org/10.1016/j.jsv.2017.10.005>.

908 ORE. Question D71: Stresses in the Rails, the Ballast and in the Formation Resulting from
909 Traffic Loads. Stresses in the formation (results of the third phase ; measurements under
910 dynamic conditions). International Union of Railways, Office for Research and Experiments;
911 1970.

912 Ramos A, Gomes Correia A, Indraratna B, Ngo T, Calçada R, Costa PA. Mechanistic-empirical
913 permanent deformation models: Laboratory testing, modelling and ranking. *Transp Geotech*
914 2020;23. <https://doi.org/10.1016/j.trgeo.2020.100326>.

915 Rollins KM, Singh M, Roy J. Simplified Equations for Shear-Modulus Degradation and
916 Damping of Gravels. *J Geotech Geoenvironmental Eng* 2020a;146:04020076.
917 [https://doi.org/10.1061/\(asce\)gt.1943-5606.0002300](https://doi.org/10.1061/(asce)gt.1943-5606.0002300).

918 Rollins KM, Singh M, Roy J, AKKOÇ B. Simplified Equations for Shear-Modulus Degradation
919 and Damping of Gravels. *J Geotech Geoenvironmental Eng* 2020b;146:04020076.
920 [https://doi.org/10.1061/\(asce\)gt.1943-5606.0002300](https://doi.org/10.1061/(asce)gt.1943-5606.0002300).

921 Sato Y. Japanese Studies on Deterioration of Ballasted Track. *Veh Syst Dyn* 1995;24:197–
922 208. <https://doi.org/10.1080/00423119508969625>.

923 Saussine G, Cholet C, Gautier PE, Dubois F, Bohatier C, Moreau JJ. Modelling ballast
924 behaviour under dynamic loading. Part 1: A 2D polygonal discrete element method
925 approach. *Comput Methods Appl Mech Eng* 2006;195:2841–59.
926 <https://doi.org/10.1016/j.cma.2005.07.006>.

927 Sayeed MA, Shahin MA. Design of ballasted railway track foundations using numerical
928 modelling. Part I: Development1. *Can Geotech J* 2018;55:353–68.
929 <https://doi.org/10.1139/cgj-2016-0633>.

930 Shan Y, Zhou S, Zhou H, Wang B, Zhao Z, Shu Y, et al. Iterative method for predicting uneven
931 settlement caused by high-speed train loads in transition-zone subgrade. *Transp Res Rec*
932 2017;2607:7–14. <https://doi.org/10.3141/2607-02>.

933 Sheng X, Jones CJC, Thompson DJ, Wu TX, Thompson DJ. A comparison of a theoretical
934 model for quasi-statically and dynamically induced environmental vibration from trains with
935 measurements. *J Sound Vib* 2003;267:621–35. [https://doi.org/10.1016/S0022-460X\(03\)00728-4](https://doi.org/10.1016/S0022-460X(03)00728-4).

937 Shenton MJ. Ballast deformation and track deterioration. *Track Technol* 1985:253–65.

938 Shih JY, Grossoni I, Bezin Y. Settlement analysis using a generic ballasted track simulation
939 package. *Transp Geotech* 2019;20:100249. <https://doi.org/10.1016/j.trgeo.2019.100249>.

940 Shih JY, Thompson DJ, Zervos A. The influence of soil nonlinear properties on the
941 track/ground vibration induced by trains running on soft ground. *Transp Geotech*
942 2017;11:1–16. <https://doi.org/10.1016/j.trgeo.2017.03.001>.

943 Suiker ASJ, de Borst R. A numerical model for the cyclic deterioration of railway tracks. *Int J*
944 *Numer Methods Eng* 2003;57:441–70. <https://doi.org/10.1002/nme.683>.

945 Thompson D. *Railway noise and vibration: mechanisms, modelling and means of control*.
946 Elsevier; 2008.

947 Wu TX, Thompson DJ. Vibration analysis of railway track with multiple wheels on the rail. *J*
948 *Sound Vib* 2001;239:69–97. <https://doi.org/10.1006/jsvi.2000.3157>.

949 Xu Q, Xiao Z, Liu T, Lou P, Song X. Comparison of 2D and 3D prediction models for
950 environmental vibration induced by underground railway with two types of tracks. *Comput*
951 *Geotech* 2015;68:169–83. <https://doi.org/10.1016/j.compgeo.2015.04.011>.

952 Yan TH, Corman F. Assessing and Extending Track Quality Index for Novel Measurement
953 Techniques in Railway Systems. *Transp Res Rec* 2020;2674:24–36.
954 <https://doi.org/10.1177/0361198120923661>.

955 Yu Z, Connolly DP, Woodward PK, Laghrouche O. Settlement behaviour of hybrid asphalt-
956 ballast railway tracks. *Constr Build Mater* 2019;208:808–17.
957 <https://doi.org/10.1016/j.conbuildmat.2019.03.047>.

958 Zhai W, Cai Z. Dynamic interaction between a lumped mass vehicle and a discretely
959 supported continuous rail track. *Comput Struct* 1997;63:987–97.

960 [https://doi.org/10.1016/S0045-7949\(96\)00401-4](https://doi.org/10.1016/S0045-7949(96)00401-4).

961 Zuada Coelho B, Varandas JN, Hijma MP, Zoeteman A. Towards network assessment of
 962 permanent railway track deformation. *Transp Geotech* 2021;29.

963 <https://doi.org/10.1016/j.trgeo.2021.100578>.

964

965 **Appendix. Vehicle mass and stiffness matrices**

966 Mass and stiffness matrices of the vehicle system:

$$[Z] = \begin{bmatrix} 0 & 0 & 0 & 0 & 0 & 0 & 1 & 0 & 0 & 0 \\ 0 & 0 & 0 & 0 & 0 & 0 & 0 & 1 & 0 & 0 \\ 0 & 0 & 0 & 0 & 0 & 0 & 0 & 0 & 1 & 0 \\ 0 & 0 & 0 & 0 & 0 & 0 & 0 & 0 & 0 & 1 \end{bmatrix} \quad (50)$$

$$[M^v] = \begin{bmatrix} Mc & 0 & 0 & 0 & 0 & 0 & 0 & 0 & 0 & 0 \\ 0 & Jc & 0 & 0 & 0 & 0 & 0 & 0 & 0 & 0 \\ 0 & 0 & Mb & 0 & 0 & 0 & 0 & 0 & 0 & 0 \\ 0 & 0 & 0 & Jb & 0 & 0 & 0 & 0 & 0 & 0 \\ 0 & 0 & 0 & 0 & Mb & 0 & 0 & 0 & 0 & 0 \\ 0 & 0 & 0 & 0 & 0 & Jb & 0 & 0 & 0 & 0 \\ 0 & 0 & 0 & 0 & 0 & 0 & Mw & 0 & 0 & 0 \\ 0 & 0 & 0 & 0 & 0 & 0 & 0 & Mw & 0 & 0 \\ 0 & 0 & 0 & 0 & 0 & 0 & 0 & 0 & Mw & 0 \\ 0 & 0 & 0 & 0 & 0 & 0 & 0 & 0 & 0 & Mw \end{bmatrix} \quad (51)$$

$$[K^v] = \begin{bmatrix} 2Ks & 0 & -Ks & 0 & -Ks & 0 & 0 & 0 & 0 & 0 \\ 0 & 2Ks \cdot lb^2 & -Ks \cdot lb & 0 & Ks \cdot lb & 0 & 0 & 0 & 0 & 0 \\ -Ks & -Ks \cdot lb & Ks + 2Kp & 0 & 0 & 0 & -Kp & -Kp & 0 & 0 \\ 0 & 0 & 0 & 2Kp \cdot lw^2 & 0 & 0 & -Kp \cdot lw & Kp \cdot lw & 0 & 0 \\ -Ks & Ks \cdot lb & 0 & 0 & Ks + 2Kp & 0 & 0 & 0 & -Kp & -Kp \\ 0 & 0 & 0 & 0 & 0 & 2Kp \cdot lw^2 & 0 & 0 & -Kp \cdot lw & Kp \cdot lw \\ 0 & 0 & -Kp & -Kp \cdot lw & 0 & 0 & Kp & 0 & 0 & 0 \\ 0 & 0 & -Kp & Kp \cdot lw & 0 & 0 & 0 & Kp & 0 & 0 \\ 0 & 0 & 0 & 0 & -Kp & -Kp \cdot lw & 0 & 0 & Kp & 0 \\ 0 & 0 & 0 & 0 & -Kp & Kp \cdot lw & 0 & 0 & 0 & Kp \end{bmatrix} \quad (52)$$

967 where Mc is mass of the car box; Mb is mass of the bogie; Mw is mass of the wheelset; Jb is
 968 the rotation inertia of the car body; Kp is the complex stiffness of the primary suspension;
 969 Ks is the complex stiffness of the secondary suspension; lb is half the distance between the
 970 bogie's centre of gravity; and lw is half the wheelbase that shares the same bogie. Kp and
 971 Ks are defined as:

$$Kp = k_{pri} + i\omega c_{pri} \quad (53)$$

$$Ks = k_{sec} + i\omega c_{sec} \quad (54)$$

972 where k_{pri} is the spring stiffness of the primary suspension; k_{sec} is the spring stiffness of
 973 the secondary suspension; c_{pri} is the viscous damping of the primary suspension; and c_{sec} is
 974 the viscous damping of the secondary suspension.

975

976